We are IntechOpen,
the world's leading publisher of
Open Access books
Built by scientists, for scientists

4,800
Open access books available

122,000
International authors and editors

135M
Downloads

154
Countries delivered to

Our authors are among the

TOP 1%
most cited scientists

12.2%
Contributors from top 500 universities

BOOK CITATION INDEX
CLARIVATE ANALYTICS
INDEXED

WEB OF SCIENCE™

Selection of our books indexed in the Book Citation Index
in Web of Science™ Core Collection (BKCI)

Interested in publishing with us?
Contact book.department@intechopen.com

Compact Antenna with Enhanced Performances Using Artificial Meta-Surfaces

Tong Cai, He-Xiu Xu, Guang-Ming Wang and Jian-Gang Liang

Abstract

In recent years, artificial meta-surfaces, with the advantages of smaller physical space and less losses compared with three-dimensional (3D) metamaterials (MTM), have intrigued a great impetus and been applied widely to cloaks, subwavelength planar lenses, holograms, etc. Typically, one most important part for meta-surfaces' applications is to improve the performance of antennas. In this chapter, we discuss our effort in exploring novel mechanisms of enhancing the antenna bandwidth using the magneto-electro-dielectric waveguided meta-surface (MED-WG-MS), achieving circular polarization radiation through fractal meta-surface, and also realizing beam manipulation using cascaded resonator layers, which is demonstrated from aspects of theoretical analysis, numerical calculation, and experimental measurement. The numerical and measured results coincide well with each other. Note that all designed antenna and microwave devices based on compact meta-surfaces show advantages compared with the conventional cases.

Keywords: magneto-electro-dielectric waveguided meta-surface, fractal meta-surface, gradient phase meta-surface, miniaturization, beam manipulation, bandwidth enhancement

1. Introduction

Microstrip antennas have been used widely in recent wireless communication systems due to their coplanar structures, easy fabrication, and stable performances. However, conventional microstrip antennas face huge challenges, such as large size, narrow bandwidth, and inconvenient tuning of the working frequency.

INTECH
open science | open minds

Recently, artificial meta-surfaces, planar inhomogeneous metamaterials composed of carefully selected elements with specific electromagnetic (EM) responses, have attracted much attention due to their strong abilities to control the wavefront of transmitted and reflected EM waves. With the unique EM properties, meta-surfaces have found a lot of applications in focusing lens, cloaks, absorbers, antennas, and other microwave devices. One of the most important applications is to improve the performances of antenna, such as extending the working bandwidth and realizing circularly polarization radiation.

In Section 1, a new concept of planar magneto-electro-dielectric waveguided meta-surface (MED-WG-MS) is introduced for the first time, which is capable of manipulating the effective permeability μ_{eff} and the effective permittivity ε_{eff} independently. As a result, the MED-WG-MS can be tuned with a larger refractive index and larger wave impedance, which is essential to realize antenna miniaturization and bandwidth enhancement, respectively. Based on the derived principle of the MED-WG-MS, a meta-surface antenna working at 3.5 GHz is proposed by properly using the MED-WG-MS. The designed antenna, occupying an area of only $0.20\ \lambda_0 \times 0.20\ \lambda_0$, realizes a series of advantages such as a 42.53% miniaturization compared with the conventional patch antenna, a 207% impedance BW enhancement, and also comparable far-field performances. In Section 2, a novel method to design the circularly polarized antenna is proposed using a combination of fractal meta-surface and fractal resonator. We find that fractal reactive impedance surface (RIS), i.e., Hilbert-shaped RIS, can reduce the substrate thickness and improve the front-to-back ratio of the antenna. More importantly, fractal resonator, i.e., Wunderlich-shaped fractal complementary split ring resonator (WCSRR), is able to achieve the CP property and further size reduction. A CP antenna working at the Wimax band is experimentally engineered with a compact layout, a relative wide axial ratio (AR) bandwidth, and a comparable radiation gain. In Section3, an ultra-thin transmissive gradient phase meta-surface (TGMS) is proposed based on the generalized Snell's law of refraction. The polarization-controlled property of the local element is demonstrated. An ultra-thin polarization beam splitter (PBS) working at the X-band is implemented by a specially designed 2D TPGM and is launched by a wideband horn antenna from the perspective of high integration, simple structure, and low cost. The polarized splitting ratio, indicating the separation level of reflected beams, is proposed and measured to systematically evaluate the performances of PBS. Finally, we summarize the chapter simply in the last section.

2. Compact microstrip antenna with enhanced bandwidth using planar MED-WG-MS

Microstrip patch antennas are experimentally demonstrated with a lot of advantages, such as coplanar configuration, simple design, and low cost, which have widespread applications in a wireless communication system recently. However, the conventional microstrip antenna is electrically large, resulting from that the working frequency is exclusively dependent on the antenna size, which limited a further application of the patch antenna. Moreover, the antenna suffers from an intrinsically narrow bandwidth (BW). To address these issues, electromagnetic (EM) meta-surfaces (MSs) have been proposed in recent years. Due to their strong EM

abilities in improving the performances of conventional devices, MS antenna has become a research hotspot with remarkable achievements. However, using the MSs to increase the impedance BW of an electrically smaller microstrip patch antenna is still rarely reported.

Artificial magneto-dielectric substrate has been verified to be a promising avenue to reduce the antenna size and extend the working band width [1–4]. A reported patch antenna, using a magneto-dielectric substrate, achieves a relative 3.2% BW ordered by 6 dB return loss. However, the antenna suffers from a high profile, which is difficult for integration in compact devices. A magneto-dielectric substrate using an embedded meander line (EML) is proposed in reference [5]. A patch antenna based on this substrate realizes an antenna miniaturization and a BW improvement. Unfortunately, it needs an additional shield metal plate that complexes the fabrication. Therefore, it is an essential issue to design an MS antenna realizing simultaneously size reduction, BW extension, and also flexible frequency turning. In this section, we explored an improved strategy to simultaneously address aforementioned issues. An electrically smaller MS element is proposed by combining the electro-dielectric and magneto-dielectric waveguided substrates, defined as the magneto-electro-dielectric waveguided MS (MED-WG-MS) [6]. The MED-WG-MS provides a freedom to control the wave impedance and refractive index simultaneously, achieving antenna miniaturization, bandwidth enhancement, and also flexible frequency modulation.

2.1. The concept and working mechanism of MED-WG-MS

As discussed in reference [5], planar WG-MS is a special kind of artificial material residing in the planar waveguide environment, which is made up of an upper metallic layer and a lower ground plane. By introducing electric and magnetic resonators in the upper and lower metallic layers, MED-WG-MS is composed, which would bring about a series of interesting characteristics, including EM manipulation, further miniaturization, and also bandwidth enhancement. In addition, the MED-WG-MS is able to tune the working frequency easily, since more freedom is provided by the element. In other words, the antenna can work at any frequency just by manipulating the electric or magnetic resonators.

Then, we will discuss about the working mechanisms of the MED-WG-MS. There is a link between the patch size and the refractive index of the used substrate for a conventional patch antenna, which can be calculated as Eq. (1a) [7], where ε_{ref} is the effective permittivity of the substrate. The quality factor Q is inversely proportion to the working bandwidth. The Q of a microstrip antenna is written as Eq. (1c), here G_r denotes the radiation conductance. For an MS antenna, with a tunable effective permeability μ_{eff} and the effective permittivity ε_{eff}, the basic principle is almost the same as the conventional counterpart. The length and quality factor of this MS antenna can be calculated in Eqs. (1b) and (2b) [6].

$$L_{ref} \approx \frac{c}{2 f_0 \sqrt{\varepsilon_{ref}}} = \frac{c}{2 f_0 n_{ref}} \tag{1a}$$

$$L_{MS} \approx \frac{c}{2 f_0 \sqrt{\varepsilon_{eff} \mu_{eff}}} = \frac{c}{2 f_0 n_{eff}} \tag{1b}$$

$$Q_{ref} = \frac{\pi\, w_p}{4\, G_r\, h\, \eta_{ref}} = \frac{\pi\, w_p \sqrt{\varepsilon_{ref}}}{4\, G_r\, h\, \eta_0} \tag{2a}$$

$$Q_{MS} = \frac{\pi\, w_p}{4\, G_r\, h\, \eta_{eff}} = \frac{\pi\, w_p \sqrt{\varepsilon_{eff}}}{4\, G_r\, h\, \eta_0 \sqrt{\mu_{eff}}} \tag{2b}$$

Therefore, normalized with the conventional patch antenna, the compact factor (CF), defined as the ratio between the patch size for the conventional antenna and the MS antenna, can be derived from Eq. (1a) and (1b) as

$$CF = \frac{n^2_{ref}}{n^2_{eff}} = \frac{\varepsilon_{ref}}{\varepsilon_{eff}\,\mu_{eff}} \tag{3}$$

The BW improving factor (BIF), evaluated by the BW ratio between the conventional antenna and the MS antenna, can be calculated as

$$BIF = \frac{Q_{ref}}{Q_{MS}} = \frac{\eta_{eff}}{\eta_{ref}} = \frac{\sqrt{\varepsilon_{ref}\,\mu_{eff}}}{\sqrt{\varepsilon_{eff}}} \tag{4}$$

Based on Eqs. (1)–(4) [6], CF and BIF can be controlled by manipulating the material parameters ε_{eff} or μ_{eff}. Our goal in this section is to achieve a smaller CF and a larger BIF to improve the patch antenna performance. The reported magneto-dielectric substrate [1, 4] is just a special case for manipulating the parameter μ_{eff}, however, the proposed MED-WG-MS in this chapter can control both ε_{eff} and μ_{eff} simultaneously.

2.2. The circuit model and EM property of MED-WG-MS

Based on the analysis in Section 1.1, we proposed a basic element as shown in **Figure 1(a)** [6]. The element is a well-known sandwich structure, consisting of an upper metallic two-turn
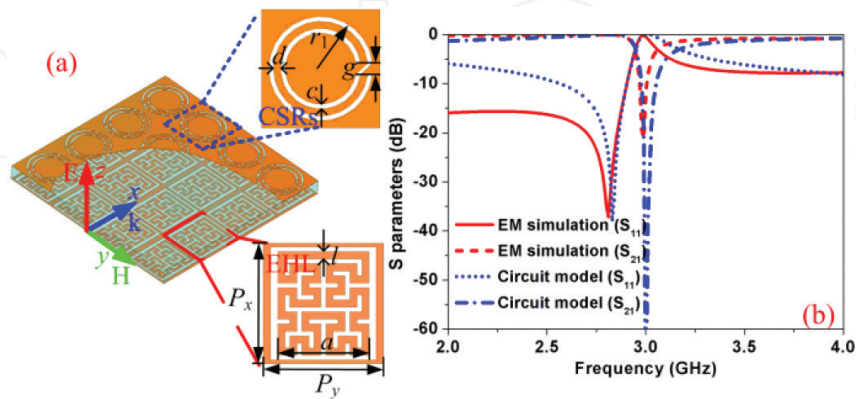

Figure 1. Schematic of the basic MED-WG-MS cell as well as the calculated S-parameters [6]. (a) Perspective view of the proposed element and the geometrical parameters (with the unit in mm); (b) S-parameters of the basic element based on the EM simulation and circuit model calculation. The detailed parameters of the CSR and EHL are $p_x = p_y = 5$ mm, $a = 3.6$ mm, $l = 0.3$ mm, $r_1 = 2.1$ mm, $d = 0.3$ mm, $c = 0.2$ mm, $g = 0.4$ mm. The circuit parameters are extracted as $C_0 = 0.11$ pF, $L_{EHL} = 17.13$ nH, $C_{CSR} = 1.21$ pF, $L = 0.34$ nH and $C = 8.09$ pF.

complementary spiral ring resonator (CSR) and a lower embedded Hilbert-line (EHL) resonator, separated by a 1.5-mm-thick F4B spacer (dielectric constant ε_r = 2.65 and the loss tangent tan δ = 0.001).

The meta-surface, composing of a periodic element, is shined with a plane wave as the E-field polarized along the z-direction and propagation along the x-direction, as the simulation set-up shown in **Figure 1(a)**. For a systematical analysis of the basic element, we proposed the effective circuit model shown in **Figure 2**. Under a waveguide circumstance, the conventional sandwich structure (composing of metallic layers and a dielectric spacer) can be represented by a parallel resonant tank (consisting of an inductor L and a capacitor C) and a parallel shorted capacitor C_0. The MD-WG-MS is designed by introducing the magnetic EHL in the ground plane of the basic element. A fractal EHL can be used effectively to control the ε_{eff} of the material. As a result, an additional inductor L_{EHL} is added in the parallel branch to represent the effect of the EHL as shown in **Figure 2(a)** [6]. An ED-WG-MS is composed of etching a two-turn complementary spiral ring resonator (CSR) in the upper metallic layer, as shown in **Figure 2(b)**. CSR has been demonstrated with compact size and electric resonant property in references [8, 9], which is suitable to tune the permeability μ_{eff}. And an additional capacitor C_{CSRs} is added in the series branch of the circuit model. By integrating the effect of the CSR and EHL, a new MED-WG-MS is designed with the structure shown in **Figure 2(c)**. Consequently, the circuit model can be obviously obtained as shown in **Figure 2(c)**. Further analysis shows that the permeability μ_{eff} is decided by the series branch, whereas the permittivity ε_{eff} is decided by the shunt branch. In other words, both material parameters μ_{eff} and ε_{eff} can be individually manipulated by adjusting the geometrical parameters of the EHL and CSR. For characterization, we obtain the EM performance of the element by using the finite element method (FEM)-based commercial software Ansoft HFSS, and the circuit parameter by using the Ansoft Serenade. **Figure 1(b)** illustrates the calculated S-parameters by EM simulation and circuit simulation as a function of frequency. There is a reasonable agreement between them, indicating a rationality of the circuit model. As can be seen, band gaps at about 3 GHz are clearly observed.
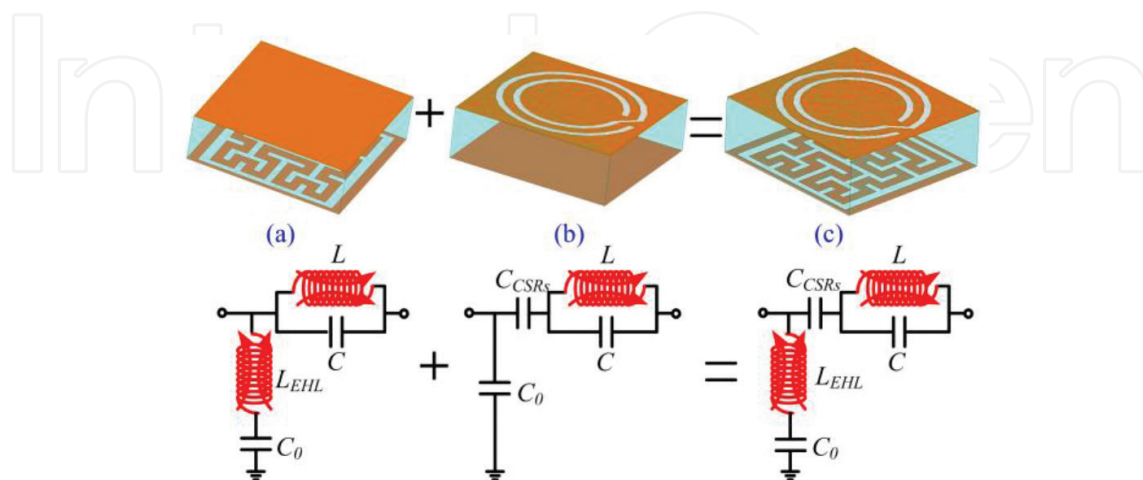

Figure 2. The evolution of WG-MS and the relative equivalent circuit model [6]. (a) MD-WG-MS, (b) ED-WG-MS, and (c) MED-WG-MS.

Next, we extracted the effective constitutive material parameters of four types of WG-MSs using the standard retrieval process [10, 11] based on the calculated S-parameters; the results are shown in **Figure 3**. With introduced CSR structures, electric resonances (about 2.86 GHz) are observed clearly for the MED-WG-MS, 90°-rotated MED-WG-MS and ED-WG-MS cases. However, by inserting EHL, magnetic resonances (about 2.95 GHz) can be seen for the MED-WG-MS, 90°-rotated MED-WG-MS, and MD-WG-MS structures. Routinely, the corresponding antiresonances in vicinity of these resonant frequencies are also appeared in the curves of material parameters, resulting from the magneto-electric coupling among cells and the finite size of the periodic structure [12]. The losses of these elements, represented by the imaginary part of the material parameters, can be ignored in all cases. Due to the anisotropic property of the proposed MED-WG-MS element, there is a slight resonant frequency shift and a small difference between the material parameters for the element and its 90°-rotated counterpart. A comparison of the material parameters indicates that the CSR can realize a manipulation of ε_{eff} and EHL accounts for the control of μ_{eff}. As is expected, according to Eqs. (3) and (4), a desirable combination of a smaller ε_{eff} with flat slope and a larger μ_{eff} is
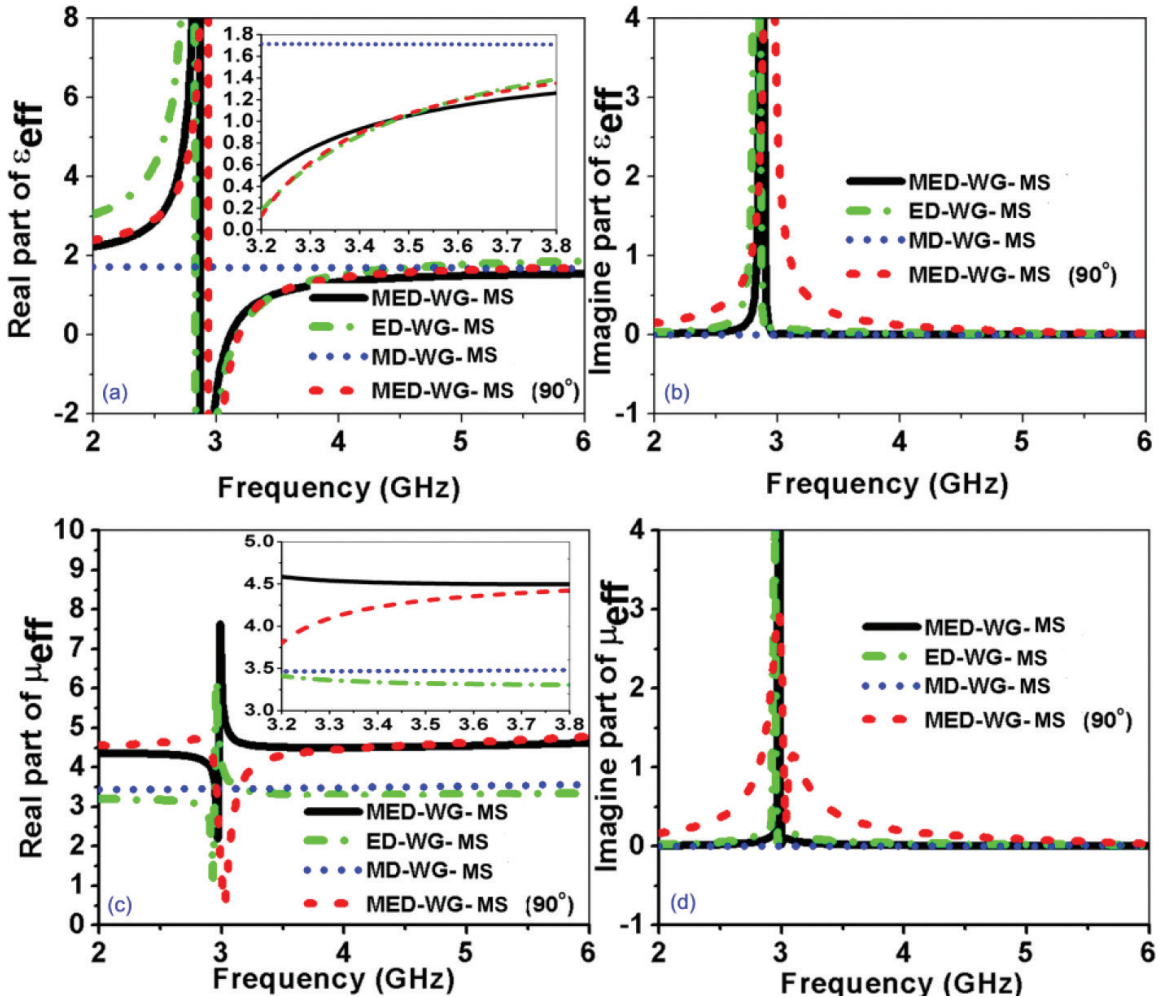

Figure 3. The effective material parameters for four different MS cells. (a) The real part and (b) imaginary part of the permittivity ε_{eff}; (c) the real part and (d) imaginary part of the permeability μ_{eff}.

obtained for the proposed MED-WG-MS element. The good performances of the designed element indicate that it is capable of improving the antenna bandwidth and reducing the antenna size. However, undesirable small μ_{eff} and large ε_{eff} are obtained for the MD-WG-MS. While small μ_{eff} and ε_{eff} with a sharp slope are obtained for the ED-WG-MS structure. Both of the ED-WG-MS and MD-WG-MS elements are not able to improve the performance of the bandwidth and reduce the structure dimension.

2.3. Design of compact microstrip antenna with enhanced bandwidth

With a desirable MED-WG-MS element in hand, we can obtain effective parameters μ_{eff} = 4.5 + j0.025 and ε_{eff} = 1.05 + j0.033 at 3.5 GHz, according to the aforementioned analysis. Upon introducing these effective parameters into Eqs. (3) and (4), CF = 0.41 and BIF = 2.87 can be calculated, which are fascinating for a patch antenna realizing size miniaturization and BW enhancement simultaneously. For proof of the analysis, we design and optimize a microstrip antenna working at 3.5 GHz by loading the MED-WG-MS elements. At frequency of 3.5 GHz, the radiator length of a patch antenna can be estimated as $L_{MS} \approx 20$ mm based on Eq. (1). The MED-WG-MS element occupies an area of $p_x \times p_y$ = 5 mm × 5 mm, therefore, a total of 4 × 4 elements are chosen in the final antenna design, with the schematic shown in **Figure 4** [6]. In the ground plane, 8 × 6 EHL cells are stacked to maintain a constant current. Moreover, the ground just under the feed-line remains unetched to guarantee the continuity of the input energy.

Frequency tuning is essential in determining the antenna performances. In the following part, we will derive a three-step frequency tuning method to achieve a flexible frequency tuning property. First, a coarse control over the operating frequency is considered by changing the outer radius r_1 of the CSR structure. As r_1 varies from 1.8 to 2.2 mm in steps of 0.1 mm, **Figure 5(a)** depicts the frequency-dependent reflection coefficients [6]. To ensure a fair comparison, the residual geometrical parameters of the CSR are kept as $p_x = p_y$ = 5mm, d = 0.3 mm,
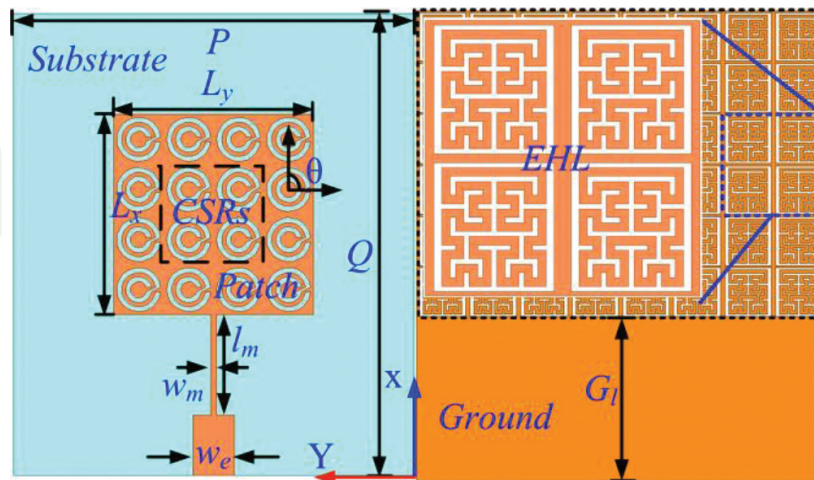

Figure 4. Schematics of the proposed antenna with MED-WG-MS loading [6]. (a) Top view; (b) bottom view. The geometrical parameters (in mm) of the proposed patch antenna are as: P = 40 mm, Q = 45 mm, $L_x = L_y$ = 20 mm, G_l = 15 mm, l_m = 10 mm, w_m = 0.8 mm, w_e = 4.1 mm; the final geometrical parameters of CSRs are r_1 = 2.1 mm, d = 0.5 mm, c = 0.3 mm, and g = 0.5 mm.
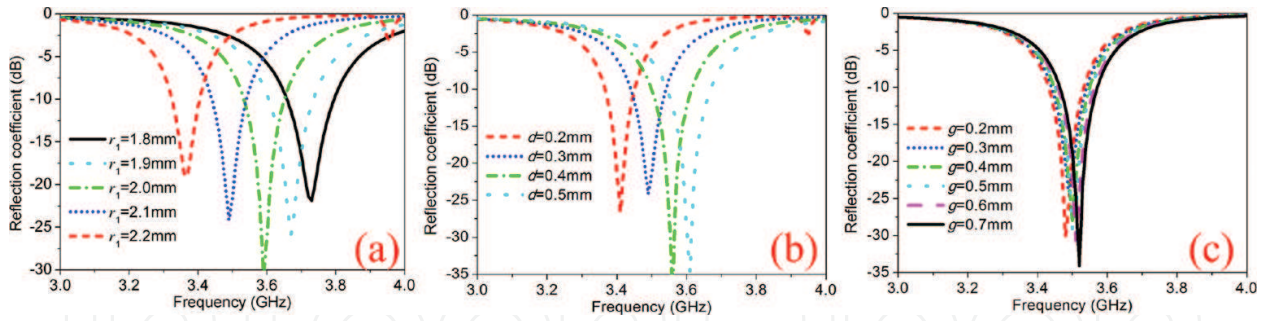
Figure 5. Simulated reflection coefficients against frequency [6]. The dependence of reflection coefficients on parameters (a) r_1, (b) d, and (c) g.

c = 0.2 mm, g = 0.4 mm. The valleys of reflection coefficients shift from 3.35 to 3.72 GHz as r_1 changes. In all cases, good impedance-matching performances are obtained for all cases with the reflection better than 19 dB. Second, a fine control over the operating frequency is studied as the parameter d increases from 0.2 to 0.5 mm. Here, the value d determines the inner circle size of CSR. Referring to **Figure 5(b)**, the reflection valleys undergo a continuous blue shift, changing from 3.4 to 3.6 GHz. Third, **Figure 5(c)** plots the reflection coefficients with a tunable parameter g. It can be seen clearly that only a small resonant frequency shift (3.47 to 3.53 GHz) appear as g varies from 0.2 to 0.7 mm. Therefore, the parameter g affords an exact control over the operating frequency. It is worth noting that the proposed three-step frequency tuning method provides a comprehensive guideline in designing antenna with an exact working frequency. Compared with the conventional patch antenna, the working frequency can be controlled easier by using the derived method.

The bianisotropic response of the CSR has a large effect on the antenna behavior. By rotating the gap orientation θ from 0 to 180°, **Figure 6(a)** plots the reflection coefficients against frequency. As θ is 90°, best performances of the antenna with wider bandwidth and lower return loss are obtained. A slightly changing resonant frequency results from the different interactions between the EHL and the CSR with different gap orientations. Here, the dependence of antenna performances on different kinds of WG-MSs is also investigated, as the results shown in **Figure 6(b)**. Desirable antenna performances of size reduction and BW enhancement are
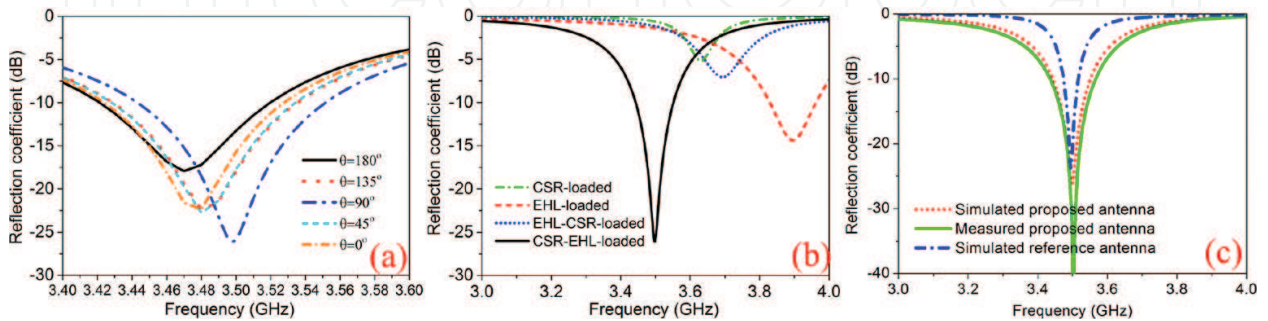

Figure 6. Simulated and measured S-parameters against frequency [6]. The dependence of S-parameters on parameters (a) θ and (b) different kinds of WG-MSs loading. (c) The final simulated and measured results for the reference and proposed antenna.

obtained for the CSR-EHL-loaded (MED-WG-MS) antenna. While for the EHL-CSR-loaded case, by etching the EHL cells in the upper patch structure and CSR elements in the ground plane, a poor impedance matching property at the resonant frequency 3.67 GHz is seen, which can be explained as the asymmetrical property of the MED-WG-MS cell along the z-direction. Therefore, we demonstrate that MED-WG-MS elements are the best choice to enhance the antenna performances.

2.4. Numerical and experimental results

With the derived three-step frequency tuning method, we can design an antenna operating exactly at frequency 3.5 GHz as shown in **Figure 4**. For experimental demonstration, we fabricate the antenna with the photograph shown in **Figure 7** [6]. The radiator of the antenna occupies an area of $L_x \times L_y = 20 \times 20$ mm^2, corresponding to $0.20 \lambda_0 \times 0.20 \lambda_0$. The size of the ground plane $P \times Q = 40 \times 45$ mm^2. For comparison, the reference antenna is also designed with a patch size of 25.4×27.4 mm^2. The fair comparison indicated that both antennas have an identical size except the radiation patch.

Then, we evaluate the reflection coefficients of the proposed antenna and the reference antenna through the ME7808A vector network analyzer. **Figure 6(c)** illustrates the results of the reflection coefficients. There is a good agreement between the simulation and measurement for the designed antenna. Both the proposed antenna and the reference antenna operate exactly at 3.5 GHz, with the numerical (experimental) resonant dips as -25(-40) dB for the designed antenna and -21.5 dB for the reference one, respectively. The simulated (measured) 10 dB impedance bandwidth is about 115 (132) MHz for the designed antenna, corresponding to 3.29% (3.77%). However, it is 43 MHz for the reference antenna. A simply calculation indicates that the BW has been enhanced significantly by 207% for the designed antenna. **Table 1** shows a detailed comparison between the two antennas, including the patch size, BW, and the values of CF and BIF. Note that the theoretical and simulated CF and BIF are in reasonable agreement with each other. The small CF = 0.57 and large BIF = 2.67 indicate that the designed antenna has the best performance compared with previous magneto-dielectric antennas [1–5]. The higher measured BIF is mainly ascribed to the random errors in measurement. To summarize, the
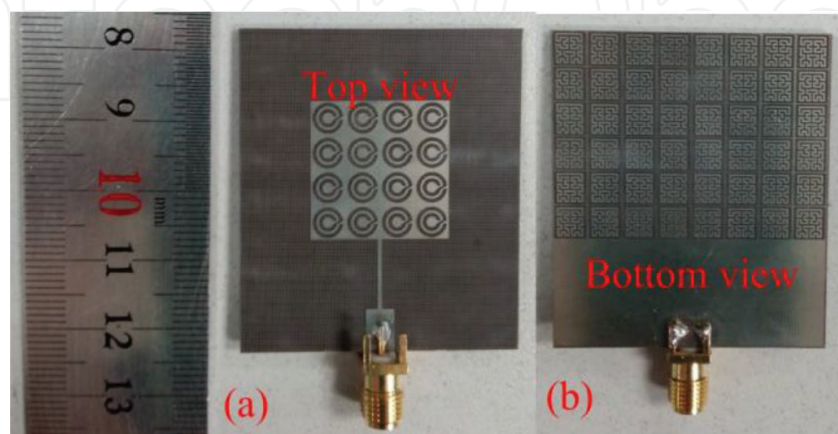

Figure 7. Photograph of the fabricated antenna [6]. (a) Top view and (b) bottom view.

Type	Size (mm²)	BW (MHz (%))	CF Theory/simulation	BIF Theory/simulation (measurement)	Antenna efficiency
Conventional patch antenna	25.4 × 27.4	43 (1.23%)	0.41/0.57	2.87/2.67 (3.07)	95.68%
Our work [6]	20 × 20	115/132 (3.29/3.77%)			93.23%

Table 1. Comparison of the reference and proposed antennas [6].

proposed MED-WG-MS element, coupled with the derived three-step working frequency method provide a guideline to design the antenna with a bandwidth enhancement at any frequency. In addition, the fabrication of the designed antenna is more convenient without using parasitic elements or metallic via holes [13, 14].

There is a link between the slope of the input admittance and the BW for an antenna. A flatter response of the input admittance means a wide impedance-matching property. **Figure 8** shows comparison of the input admittance for the designed antenna and the reference antenna [6]. It is worth noting that both the real part and the imaginary part of the input admittance for the designed antenna show a flatter response than that of the reference antenna, indicating an enhanced BW for the designed antenna.

Next, we evaluate the field distributions for both the designed antenna and the reference one. **Figure 9(a)** and **(b)** shows the comparison of the H-field distributions for both antennas [6]. There is a nearly periodic distribution for the H-field of the proposed antenna, which is attributed to the loading of the MED-WG-MS cells. More importantly, based on the material
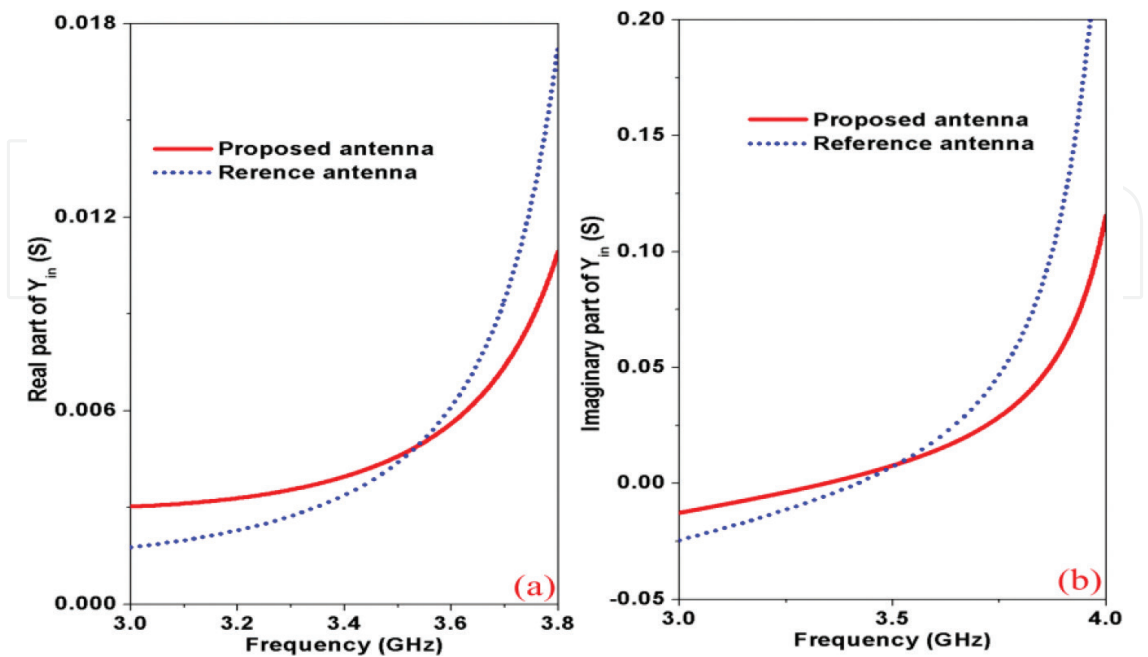

Figure 8. Simulated input admittance for both antennas [6]. (a) Real part and (b) imaginary part.
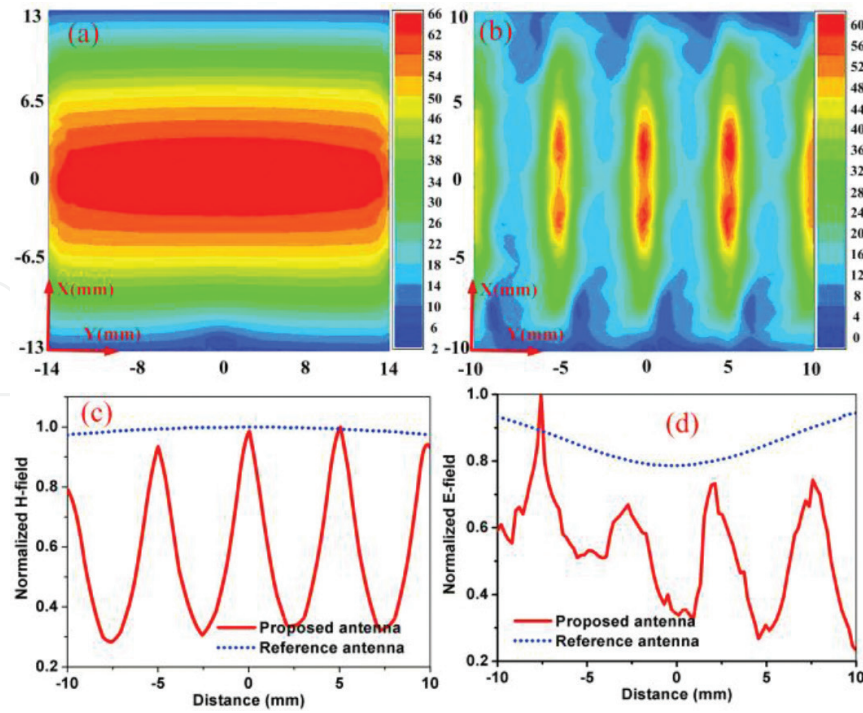
Figure 9. Field distributions for the proposed antenna and reference antenna [6]. The H-field distribution for (a) reference antenna and (b) proposed antenna; a comparison of the normalized (c) E-field intension and (d) H-field intension.

parameters, there is larger wave impedance $\sqrt{\mu_{eff}/\varepsilon_{eff}}$ for the designed antenna. The larger wave impedance induces a weaker H-field intensity and a smaller quality factor, which explained the enhancement of the BW from another aspect. The field intensity along the line $y = 0$ is also studied, as the results shown in **Figure 9(c)** and **(d)**, both the E-field and the H-field intensity are normalized to the maximum value. With the loading of the MED-WG-MS elements, the E-field, and the H-field intensity are periodic for the proposed antenna, while the distributions are almost consistent for the reference antenna. Therefore, we can conclude that the loading of MED-WG-MS elements induces a redistribution of the electromagnetic energy.

Finally, we examine the far-field radiation performances by HFSS simulation and measurement in an anechoic chamber. The three-dimensional (3D) radiation patterns at three representative frequencies (the lower frequency 3.440 GHz, the center frequency 3.5 GHz, and upper frequency 3.555 GHz) are depicted in **Figure 10(a)–(c)** [6]. Given the defects in the ground plane, seemingly bidirectional radiation patterns are observed for the three frequencies. But consistent with the conventional patch antenna, the designed one still works at TM$_{10}$ mode. The radiation patterns in both principal planes at 3.5 GHz are measured, as the results shown in **Figure 10(d)**. The level of the cross-polarization is better than -22.8 dB. Referring to the antenna gain in **Figure 10(e)**, good agreement is observed for the simulated and measured results. Within the 10 dB impedance bandwidth, the gain is higher than 4.6 dBi. Moreover, the radiation efficiency of the antenna is about 93.23%.

In summary, a new strategy of enhancing the BW and reducing the size of a patch antenna is proposed by simultaneously manipulating the material parameters μ_{eff} and ε_{eff}. For proof of
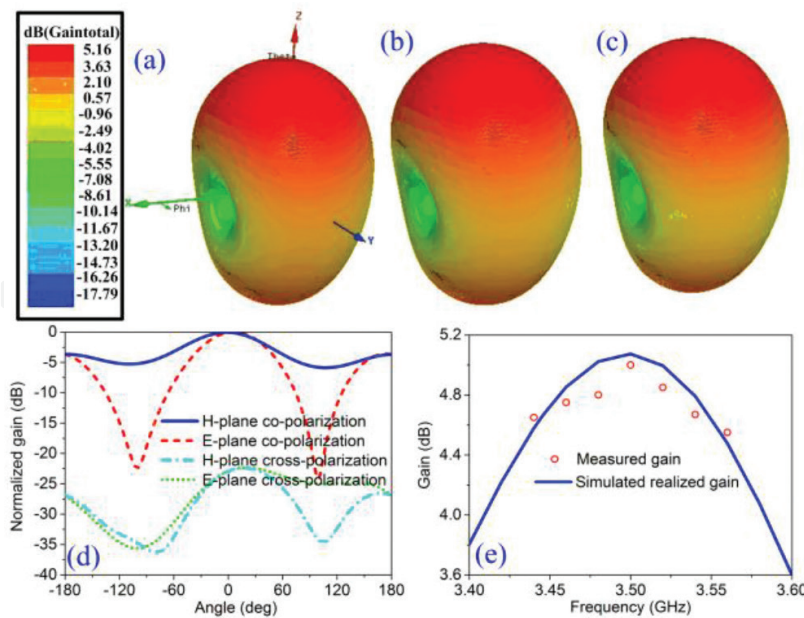
Figure 10. Radiation patterns for the designed antenna [6]. Simulated 3D radiation patterns at (a) 3.440 GHz, (b) 3.50 GHz and (c) 3.555 GHz; (d) measured 2D radiation pattern at 3.50 GHz; (e) simulated and measured antenna gain.

the concept, a MED-WG-MS element is designed to realize larger values of refractive index and wave impedance by tuning the geometrical parameters. Loading these elements in a patch antenna, about 307% BW and 42.53% miniaturization are obtained. This chapter provides a new avenue to design patch antenna with enhanced bandwidth and also compact size.

3. Miniaturized circularly polarized antenna with fractal meta-surface and fractal resonator

We have discussed about the strategy of employing MED-WG-MS element to manipulate the effective material parameters μ_{eff} and ε_{eff} in the last subsection. In this section, we explore a new scheme to realize miniaturized circularly polarized (CP) antenna with fractal meta-surface and fractal resonator. The fractal meta-surface is used to design reactive impedance surface (RIS) to improve the antenna performance in terms of reducing substrate thickness and achieving good front-to-back ratio, whereas fractal resonator with strong space-filling property achieves the CP property and further size reduction.

Unlike linearly polarized (LP) antennas, microstrip circularly polarized (CP) antennas have a stable date transmission rate regardless of the polarizations of the transmitter and the receiver, thus have found numerous applications in the recent wireless communication system [15, 16]. However, traditional CP antennas are designed by involving various perturbations (such as truncated corners), which conflicts with the miniaturization requirement and wide bandwidth applications [17, 18]. In recent years, meta-surfaces, such as reactive impedance surface (RIS), have been applied to enhance the performances of CP antennas [19–28], such as realizing miniaturization by loading RIS [20], achieving multi-frequency operation [21, 25]. However, there are never open reported techniques to reduce the profile of the CP

antenna. In this section, fractal concept has been introduced to design RIS, which realizes both miniaturization and low profile. Good performances of the designed CP antenna by using the fractal RIS are numerically and experimentally demonstrated.

First, we show the perspective view of the proposed Hilbert fractal RIS (HRIS)-inspired Wunderlich-shaped fractal complementary split ring resonator (WCSRR)-loaded CP antenna [29], as shown in **Figure 11** [29]. The antenna consists of three layers, the upper metallic radiator, the HRIS spacer, and the lower metallic ground plane. WCSRR is etched in the metallic radiator to realize both antenna miniaturization and CP wave. 6 × 6 HRIS elements are loaded
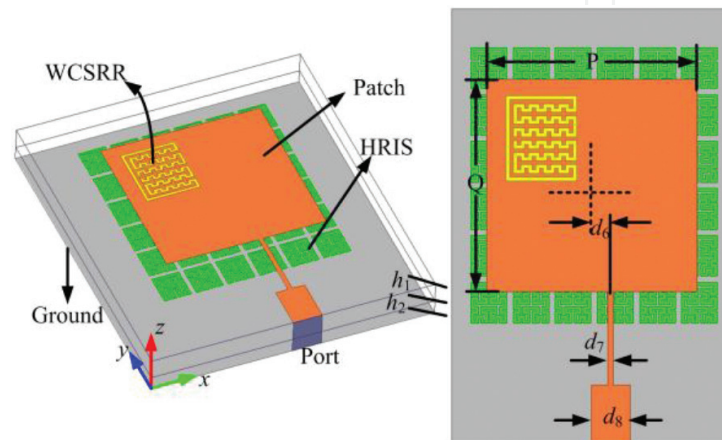

Figure 11. Topology of the proposed CP antenna based on HRIS and WCSRR slot [30]. (a) Perspective; (b) top and bottom view as well as the illustration of geometrical dimensions. The detailed geometrical parameters are listed as: $P = Q = 21.5$ mm, $h_1 = 1.5$ mm, $h_2 = 1$ mm, $d_6 = 2$ mm, $d_7 = 0.6$ mm and $d_8 = 4.1$ mm.

on the F4B substrate under the patch radiator. Two inexpensive F4B dielectric layers ($\varepsilon_r = 2.65$, $\tan\delta = 0.001$) are adopted in the proposed antenna with $h_1 = 1.5$ mm and $h_2 = 1$ mm. The overall antenna occupies a volume of 40 mm × 45 mm × 2.5 mm, and the patch radiator has a dimension of 21.5 mm × 21.5 mm. The working frequency of the antenna is chosen as 3.5 GHz (Wimax band). For characterization, we perform numerical simulations using a finite element method (FEM)-based solver Ansoft HFSS.

3.1. The EM property of the fractal RIS

RIS, proposed by Kamal et al. [22], has been used widely in antennas to reduce the radiator size and enhance the working bandwidth. In **Figure 12(a)** [29], conventional RIS (CRIS) consists of a periodic system of metallic patches ($l_a \times l_b = 4.3$ mm × 3.8 mm), 1-mm-thick F4B spacer, and a metallic ground plane. The upper substrate is introduced to support the patch radiator. In simulation, an infinite CRIS meta-surface is illuminated by transverse electric and magnetic (TEM) plane wave with the propagation vector along the z-direction and the electric field along the y-direction. Therefore, perfect electric conductor (PEC) conditions are assigned in front and back boundaries, and perfect magnetic conductor (PMC) conditions in left and right boundaries, respectively. Under this circumstance, the CRIS element can be represented by a parallel resonant tank which consists of an inductor L and a capacitor C. The
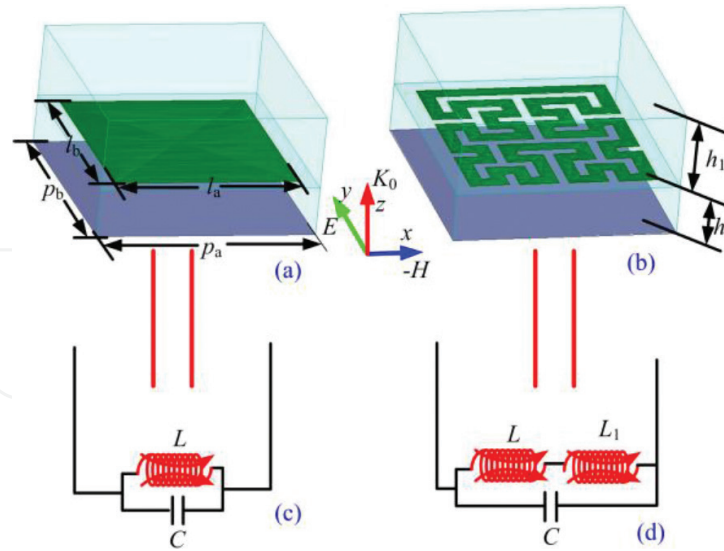
Figure 12. The topologies and equivalent circuit models of CRIS and HRIS [30]. The topologies of (a) CRIS and (b) HRIS; relative circuit model for (c) CRIS and (d) HRIS. The geometrical parameters are list as: h_1 = 1.5 mm, h_2 = 1 mm, l_a = 4.3 mm, l_b = 3.8 mm, p_a = 5 mm, p_b = 4.5 mm.

inductor L is mainly decided by the dielectric constant ε_r and the thickness h_2. While the shunt capacitor C is determined by the edge coupling between the adjacent cells. A variation of the geometrical parameters (l_a, l_b, p_a, p_b, and h_2) induces a change of the lumped circuit elements, and thus the resonant frequency. We can increase the lumped inductor L by introducing compact structures in the periodic patch, corresponding to reduce the substrate thickness h_2. For example, mushroom-like RIS increases the inductor L by digging the metallic via holes which brings about considerable losses for the concentrating currents around the holes [22]. Here, we propose the concept fractal RIS to increase the inductor L. An additional inductor L_1 is introduced to represent the EM response of the fractal structure. In fact, the fractal structure can be chosen arbitrary, e.g., the Sierpinski curve and Koch curve. Here, we adopt the Hilbert RIS, as the topology shown in **Figure 12(b)**. The value of L_1 is determined by the iteration orders (IO). **Figure 13** shows three kinds of HRISs with IO = 0, 1, and 2, respectively. Different from the traditional Hilbert fractal curve, these curves are revised by extending the start and the end points with the length of a minimum fractal segment, and then connect the terminals.
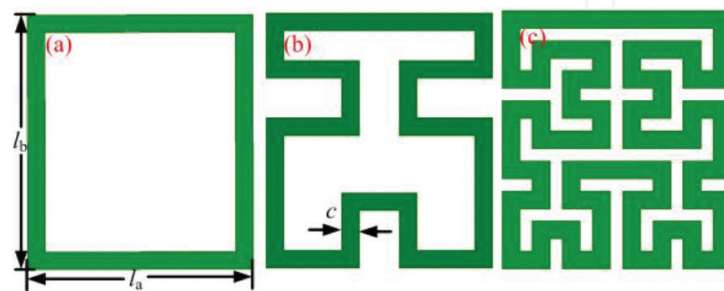

Figure 13. The revised Hilbert curves with different IOs (a) IO = 0; (b) IO = 1; (c) IO = 2 [30]. The geometrical parameters are listed as: l_a = 4.3 mm, l_b = 3.8 mm, c = 0.4 mm.

To evaluate the EM response of the HRIS, **Figure 14(a)** depicts the reflection phases of HRIS with different IOs. Note that the fair comparison is made with the geometrical parameters consistent except the IOs of the HRISs. At the resonant frequency, the reflection phase is about zero [27]. As seen from **Figure 14(a)**, the operating frequency changes from 9.1 to 7.41 GHz as IO increases from 0 to 2. The second HRIS cell occupies a dimension of $\lambda_0/8.1 \times \lambda_0/9 \times \lambda_0/16.2$, which is much smaller than the working wavelength. With a larger IO of the HRIS, stronger space-filling property of the structure is obtained, which induces a smaller resonant frequency. Here, IO = 2 is selected from the tradeoff of an easy fabrication and an electrically smaller structures. **Figure 14(b)** illustrates the dependence of reflection phase for RISs on the substrate thickness h_2. The resonant frequencies decrease as h_2 increases. It is worth noting that the HRIS with $h_2 = 1$ mm has an almost same resonant frequency with that of the CRIS with $h_2 = 2$ mm, which means a reduction of substrate thickness for the HRIS. Compared with the conventional RIS, fractal RIS has huge advantages in smaller size, lower thickness, and also easier working frequency control. Since more circuit parameters are inserted by the fractal structure, more freedom is provided to tune the working frequency.

3.2. Working principle of compact fractal resonator

With a unique EM property and a planar structure, split ring resonator (SRR), and its complementary part, CSRR have been utilized in designing microwave devices and enhancing their performances. However, it is still a great challenge to excite CP wave by integrating the fractal strategy with the CSRR structure. We combine the Wunderlich-shaped fractal structure and the CSRR (WCSRR) to achieve not only antenna miniaturization but also good CP radiation. To demonstrate the advantage of WCSRR over the traditional CSRR, the EM response of three kinds of CSRRs is compared. **Figure 15** presents the basic topologies of different SRRs, such as conventional SRR, meander-line-loaded SRR (MSRR), and WSRR. Based on the Babinet principle, we etched the CSRR, MCSRR, and WCSRR structures in the patch radiator. The reflection coefficients and axial ratio (AR) for antennas with different slots are provided in **Figure 16**. Good impedance matching property for all cases can be observed clearly by the
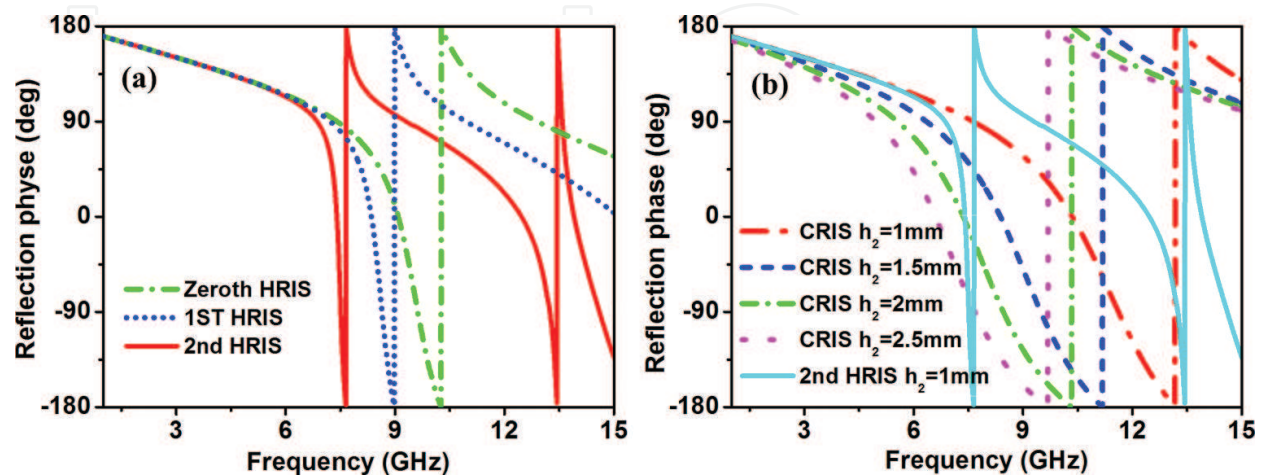

Figure 14. Numerically simulated reflection phase [30]. (a) The dependence of reflection phase on IOs; (b) the dependence of reflection phase on h_2.
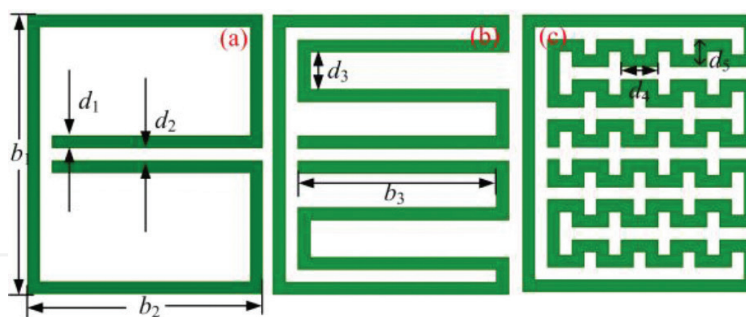
Figure 15. Schematic of the proposed revised SRRs [30]. Topology of (a) SRR, (b) MSRR and (c) WSRR as well as the illustration geometrical dimensions. The final geometrical parameters are listed as: $d_1 = d_2 = 0.4$ mm, $d_3 = 1.1$ mm, $d_4 = 1.2$ mm, $d_5 = 0.9$ mm, $b_1 = 9$ mm, $b_2 = 7.6$ mm, and $b_3 = 6.4$ mm.

resonant dips, as shown in **Figure 16(a)**. The conventional antenna without CSRR loading operates at about 3.8 GHz, whereas the center frequency reduces significantly to 3.75, 3.65, and 3.5 GHz for the CSRR-, MCSRR-, and WCSRR-loaded antennas, respectively. The extending of the current path caused by the fractal curve induces the considerable reduction of operating frequency, which is equivalent to realize antenna miniaturization working at the same frequency. **Figure 16(b)** shows the effects of CSRRs on the AR performances. Note that the slots have a significant effect on the antenna AR. An obvious linearly polarized antenna is obtained without loading CSRRs. The values of AR reduce significantly by loading CSRRs. The best performance of the CP antenna is observed by loading WCSRR, which achieves a lower operating frequency and a smaller AR value. Therefore, we can use the Wunderlich-shaped fractal slot to improve CP antenna performances.

3.3. Numerical results of a CP antenna

The feeding position as well as the slot position is very important in determining both input impedance and AR value. Antenna performances are simulated by HFSS via tuning the feeding position. The parameter d_6 increases from 0 to 3 mm in steps of 0.5 mm, the
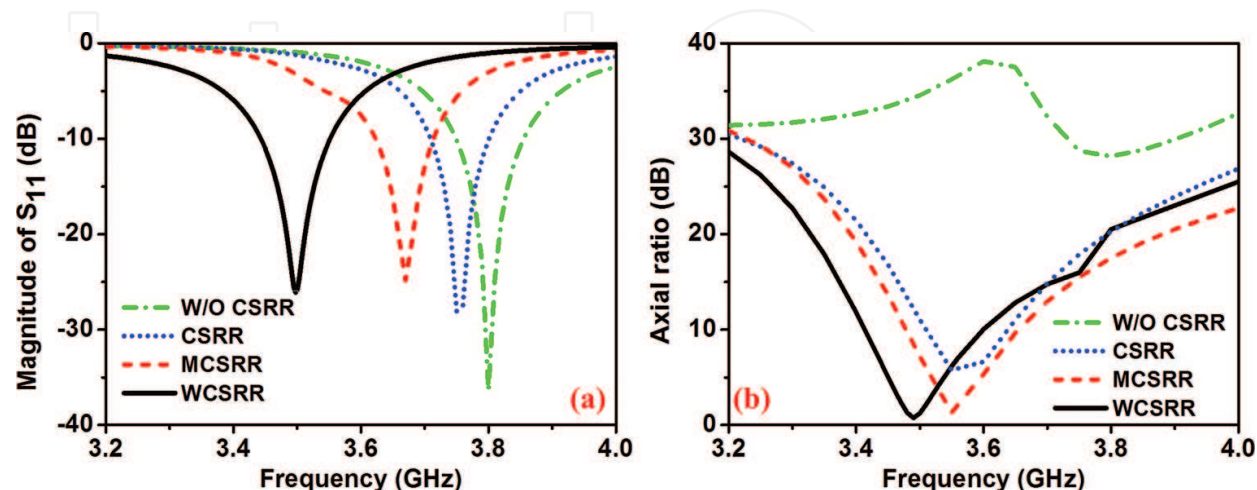

Figure 16. Simulated reflection coefficients and ARs against frequency [30]. (a) The dependence of reflection coefficients on different CSRR structures; (b) the dependence of ARs on different CSRR structures.

corresponding reflection coefficients and AR values are shown in **Figure 17**. The operating frequencies keep almost consistent when d_6 increases from 0 to 2 mm, while the impedance matching property deteriorates slightly. A slight red shift of the working frequency appears as d_6 varies from 2.5 to 3 mm. The AR has been significantly improved as d_6 increases, while the AR valleys decrease continuously from 3.52 to 3.48 GHz. As d_6 = 2 mm, both the dip of the reflection coefficient and the AR valley appear at 3.5 GHz, which is interesting and should be highlighted. **Figure 17(c)** and **(d)** shows the comparison of the magnitude ratio E_y/E_x and phase difference δ_x-δ_y as d_6 varies. Note that E_y/E_x decreases as d_6 increases, so as the δ_x-δ_y. As d_6 = 2 mm, the best performance with a flattest curve of the E_y/E_x and an exact 90° δ_x-δ_y is obtained at frequency of 3.5 GHz. Therefore, d_6 = 2 mm is selected for the final CP antenna design.

Then, we study the electric field distribution of the CP wave at 3.5 GHz, as the results shown in **Figure 18**. The electric field is mainly concentrates on the radiation patch and the WCSRR slot. Left-handed CP wave is observed clearly with a clockwise-rotated electric field. The variation of the field on the WCSRR indicates that the slot plays an essential role in exciting the CP wave. Right-handed CP wave can be excited by changing the position of the slot.
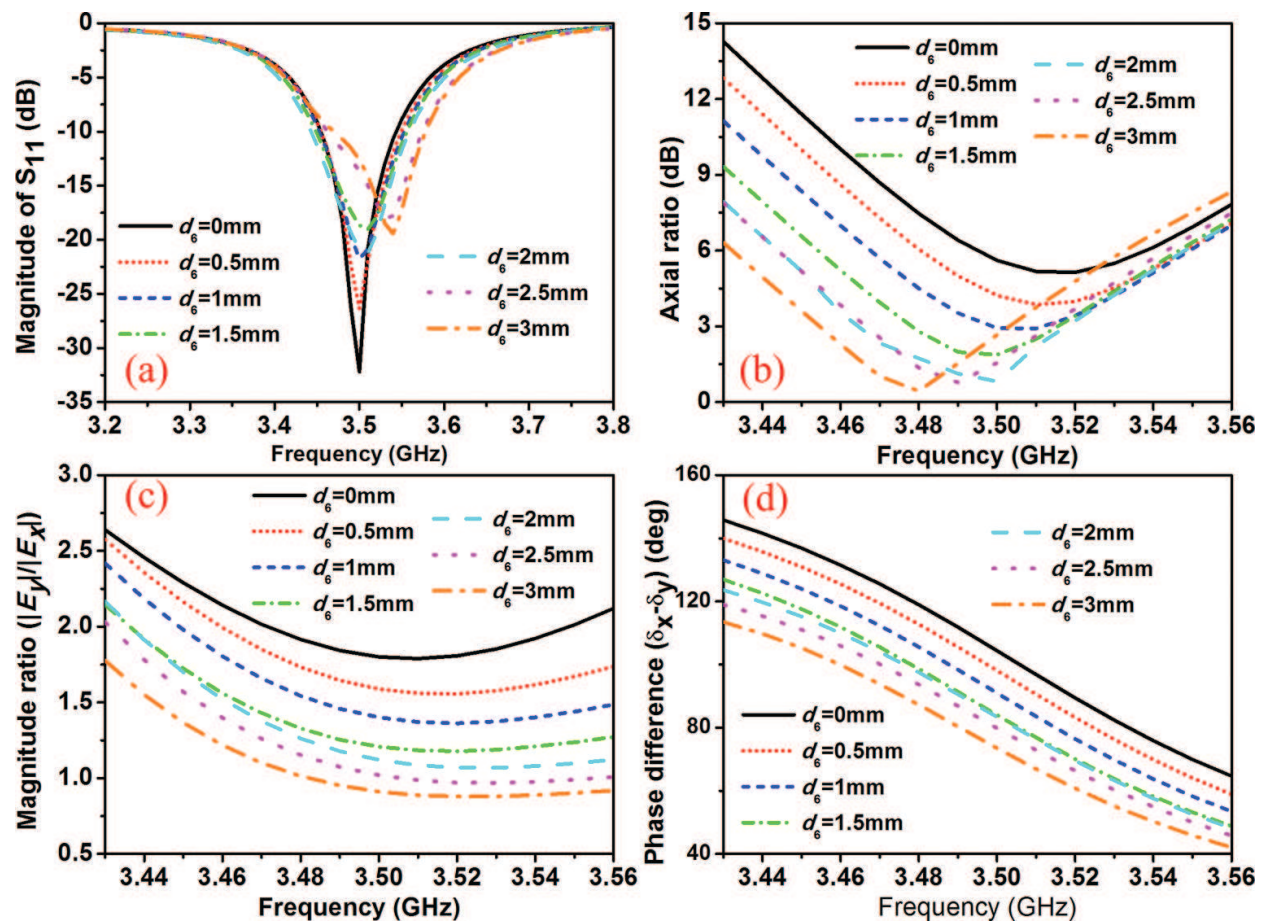

Figure 17. Simulated reflection coefficients, ARs, magnitude ratio as well as phase difference with different feeding positions [30]. The dependence of (a) reflection coefficients, (b) ARs, (c) magnitude ratio, and (d) phase difference on d_6.
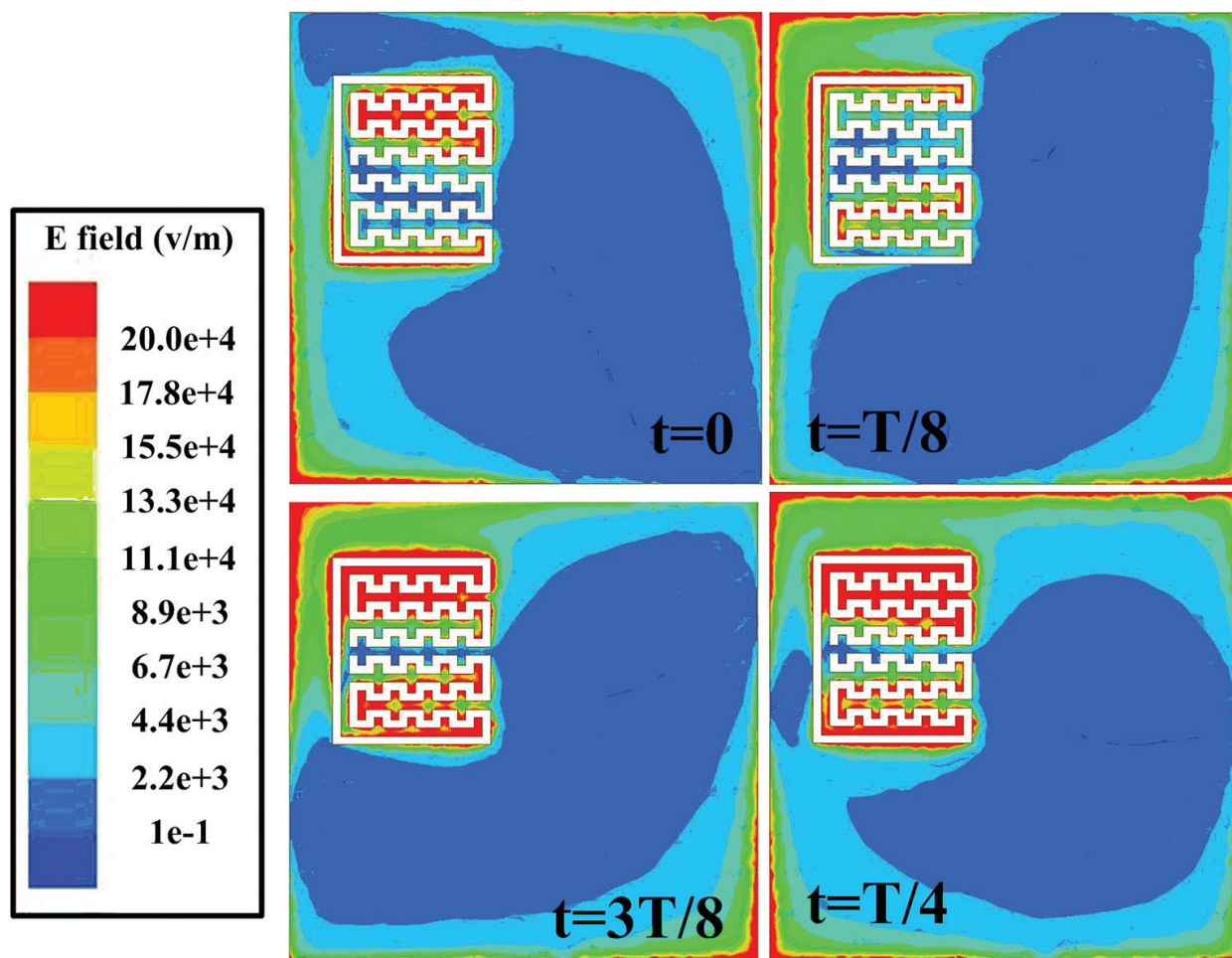
Figure 18. Electric-field distribution in the patch at 3.5 GHz in time-domain [30].

3.4. Fabrication and experimental results

For experimental demonstration, the finally double-layered CP antenna is fabricated based on a standard printed-circuit-board (PCB) technology, with the fabricated sample for the upper layer and the lower layer shown in **Figure 19**. The two layers with the same footprints are boned tightly together by an adhesive. Then we experimentally evaluate the performances of the CP antenna.
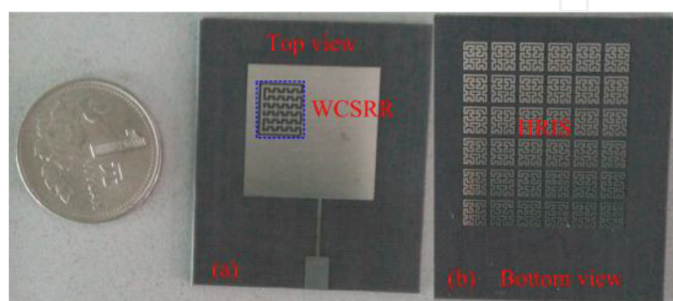

Figure 19. Photograph of the fabricated proposed antenna. (a) Top view; (b) bottom view [30].
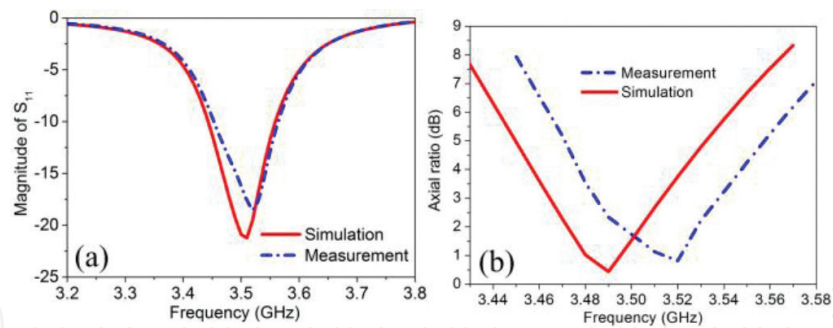
Figure 20. Simulated and measured (a) reflection coefficients and (b) ARs of the proposed CP antenna [30].

First, we examine the impedance matching property of the antenna. The reflection coefficient of the sample is measured by a vector network analyzer (ME7808A). **Figure 20(a)** depicts a comparison of the simulated and measured reflection coefficients. We can see clearly that there is an excellent agreement between the numerical and experimental results. A slight frequency shift upward about 20 MHz in the experiment is mainly attributed to the fabrication errors which is inherent and the introduction of the adhesive in the assembly process. The simulated (measured) reflection coefficient has a resonant dip of -22 dB (-18 dB) at about 3.5 GHz (3.52 GHz), respectively. The working bandwidth, characterized by the 10 dB return loss, is about 132 and 127 MHz for the simulation and measurement, respectively. The relative BW is calculated of 3.77% and 3.61%.

Then, we evaluate the AR ratio of the designed CP antenna. In the experiment, the AR is measured by the intensity ratio between Ey and Ex, which is obtained in an anechoic chamber through the far-field measurement system. As seen from **Figure 20(b)**, the 3-dB AR bandwidth for the simulated and measured results is 55 and 65 MHz, corresponding to 1.58 and 1.86%, respectively. And the minimum values of the AR are 0.41 and 0.75 for the simulated and measured results. Note that 3-dB AR BW is completely within the 10-dB impedance BW.

Finally, we measure the far-field radiation patterns in xoz and yoz planes, as the results shown in **Figure 21**. There is a good agreement between the simulation and measured results. The
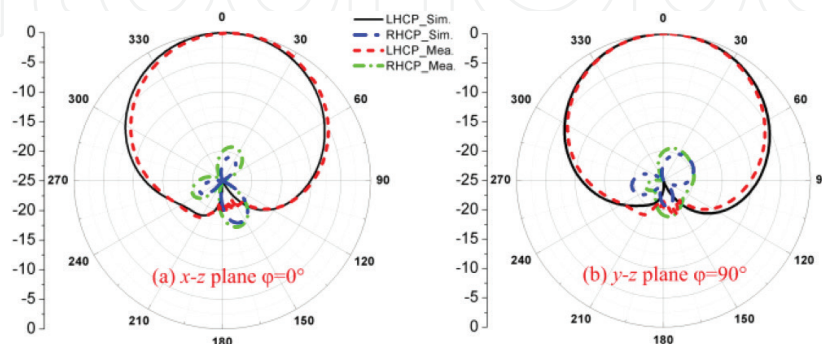

Figure 21. Simulated and measured far-field radiation patterns of the proposed CP antenna at CF in (a) x-z plane and (b) y-z plane [30].

CP wave is detected as expected. We can see clearly that the direction of the peak radiation is around the boresight direction. A pure CP wave is demonstrated for that the cross-polarization is better than 18.5 dB in both simulated and measured results, which should be highlighted. The front-to-back ratio (F/B) is larger than 15 dB in the experimental result. The radiation gain is about 6.3 dBic for both numerical and experimental results. The designed CP antenna realizes 91.5% antenna efficiency. Good radiation performances, such as good AR property and comparable antenna gain, indicate that the antenna has a potential value in the recent wireless communication system.

In summary, we have proposed a new strategy to design CP antenna by combining a fractal RIS and a fractal slot. For proof of the strategy, a CP antenna by loading HRIS structure and the WCSRR slot is designed, assembled, and measured. The experimental result coincides well with the simulated case. The antenna advances in many aspects such as a compact size (40 mm × 45 mm × 2.5 mm), good AR property (0.75 dB), and comparable radiation gain (6.3 dBic). In addition, the antenna is fabricated based on the PCB technology, free of via holes and without using the complex feeding network.

4. Ultra-thin polarization beam splitter using TGMS

Meta-surfaces, as a 2D planar inhomogeneous metamaterials, are composed of carefully selected elements with specific EM responses, have attracted much attention recently due to their strong abilities to manipulate the wavefront of transmitted and reflected EM waves. Very recently, scientists and engineers have designed functional devices by using meta-surfaces. One of the most important applications is to realize the polarization beam splitter (PBS). PBS is a typical device to manipulate the differently polarized waves independently, which has been found essential in photonics. Conventional PBSs, achieving by natural crystal birefringence [30] and 2D photonic crystals [31, 32], suffer from low efficiencies and limited splitter angle. The PBS performances have been enhanced by using the semiconductor meta-surface [33], photonic-integrated circuits [34], and 2D metamaterials [35–37]. However, these devices are electrically large and complex in fabrication. In this subsection, we propose a novel PBS based on the 2D transmissive phase gradient meta-surface (TPGM) [38]. The proposed PBS is designed based on the generalized Snell's laws, which has a low-profile about $0.1\ \lambda_0$, high transmission efficiency, and also convenient wave control.

4.1. Polarization-controlled mechanism of local element

According to the geometrical optics, the EM wave would be reflected or refracted when passing through the interface of two media. When the EM wave propagates in a uniform medium, the wave vector can be written as

$$\begin{cases} k_{xi} = 0 \\ k_{yi} = 0 \\ k_{zi} = k_0 \end{cases} \tag{5}$$

where k_{xi} represents the wave-vector along the x-direction and k_0 is the propagation constant. The generalized laws of reflection and refraction, derived from the Fermat's principle, indicate that the anomalous reflection or refraction phenomenon can be observed at the interface when the phase discontinuity exists [39]. At the same time, the EM response of the GMS is independent when excited with differently polarized waves. Illuminated by a normally incident EM wave along the z-direction with the electric field along the i-direction (x- or y-direction), the wave vector of the transmission can be calculated as

$$\begin{cases} k_{(x,t)}^{(\hat{i})} = \xi_x(i) \\ k_{(y,t)}^{(\hat{i})} = \xi_y(i) \\ k_{(z,t)}^{(\hat{i})} = \sqrt{k_0^2 - (k_{(x,r)}^{(\hat{i})})^2 - (k_{(y,r)}^{(\hat{i})})^2} \end{cases} \quad (6)$$

where the superscript i denotes the incident polarization $\vec{E}//\vec{x}$ or $\vec{E}//\vec{y}$ (horizontal and vertical polarizations, $E_{//}$ or $E_\wedge$). $\xi_x^{(i)}$ represents that the gradient along the x-direction while the incident polarization is along the i-direction.

For the practical GMS, the phase gradient can be calculated as

$$\begin{cases} \xi_x(x) = \dfrac{\partial \varphi_x(x,y)}{\partial x}, & \xi_y(x) = \dfrac{\partial \varphi_x(x,y)}{\partial y} \\ \xi_x(y) = \dfrac{\partial \varphi_y(x,y)}{\partial x}, & \xi_y(y) = \dfrac{\partial \varphi_y(x,y)}{\partial y} \end{cases} \quad (7)$$

According to Eq. (7), two points should be highlighted. First, the phase distribution φ at the position (x, y) can be controlled by both the geometrical structuring and the polarization of the incident EM wave. Second, the phase gradient ξ is determined by the phase distribution $\varphi(x, y)$ at different directions. The phase distribution $\varphi(x, y)$ and the phase gradient ξ provide a powerful freedom to manipulate the EM wave, simultaneously.

Based on Eq. (7), a transmissive PBS can be realized by controlling the parameters $\xi_x(x)$ and $\xi_y(y)$ independently. In other words, we can manipulate the transmission phase $\varphi_x(x, y)$ and $\varphi_y(x, y)$ to achieve desirable gradients ($d\varphi_x/dx$ and $d\varphi_y/dy$) along the x- and y-directions, respectively. According to the generalized Snell's law, the refraction angles to horizontal and vertical polarizations can be calculated as

$$\begin{cases} \theta_{t//} = \arcsin(\dfrac{\lambda_0}{2\pi}\dfrac{d\varphi_x}{dx}) \\ \theta_{t_\perp} = \arcsin(\dfrac{\lambda_0}{2\pi}\dfrac{d\varphi_y}{dy}) \end{cases} \quad (8)$$

To make the principle of the PBS clear, **Figure 22** provides the schematics of anomalous refractive phenomena in four different conditions. 2D TPGMs, positioned at the xoy plane with different phase distributions, are shined by hybrid EM waves along the z-direction, respectively. As seen from **Figure 22(a)**, TPGM1 has no phase gradient along the x- and
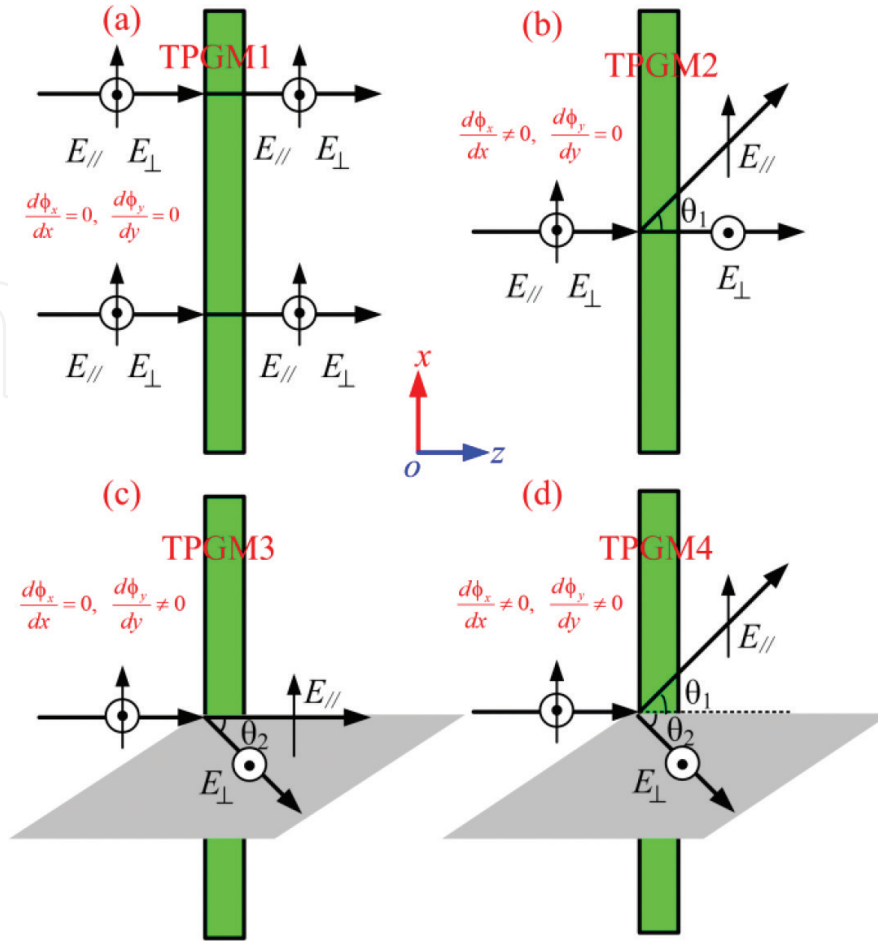
Figure 22. Anomalous refractive effects when 2D TPGMs with different phase distributions are illuminated by the hybrid EM waves [38]. Schematics of the hybrid EM waves passing through (a) the TPGM1 with $d\varphi_x/dx = d\varphi_y/dy = 0$, (b) the TPGM2 with $d\varphi_x/dx \neq 0$ and $d\varphi_y/dy = 0$, (c) the TPGM3 with $d\varphi_x/dx = 0$ and $d\varphi_y/dy \neq 0$, and (d) the PGM4 with $d\varphi_x/dx \neq 0$ and $d\varphi_y/dy \neq 0$.

y-directions ($d\varphi_x/dx = d\varphi_y/dy = 0$). Based on the Fermat's principle, the transmitted wave propagates along the z-direction, and the hybrid EM waves cannot be separated. For the TPGM2 with a phase gradient in the x-direction ($d\varphi_x/dx \neq 0$) and consistent phase distribution along the y-direction ($d\varphi_y/dy = 0$), the horizontally polarized wave deflected to an angle θ_1, while the vertical polarization wave propagates along the z-direction. The vertical polarization wave can be deflected to angle θ_2 for the TPGM3 with phase gradient existing only along the y-direction ($d\varphi_x/dx = 0$, $d\varphi_y/dy \neq 0$), as shown in **Figure 22**(c). As expected, hybrid EM waves can be deflected to angles θ_1 and θ_2 when passing through the TPGM4 with phase gradients along the x- and y-directions ($d\varphi_x/dx \neq 0$, $d\varphi_y/dy \neq 0$). Here, θ_1 and θ_2 are determined by Eq. (8). Therefore, we can realize an arbitrary splitting angle by carefully optimizing the phase distributions on TPGM.

4.2. High-efficiency transparent principle of the transmissive element

For the first step, we should find a transparent element not only with a high transmission coefficient but also a changeable transmission phase. In general, a complete phase shift range
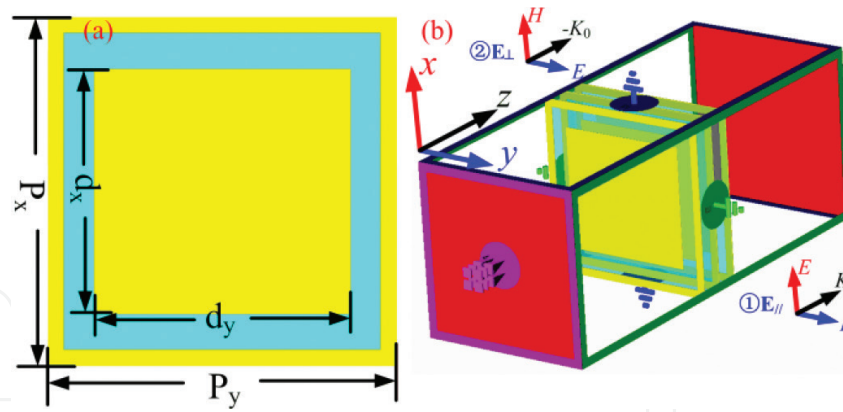
Figure 23. The topology and simulation setup for the proposed tri-player cascaded sub-unit cell [38]. (a) The top view of the subunit cell as well as the geometrical parameters; (b) simulation setup for differently polarized waves.

over 360° is required to guarantee a free wavefront control. Note that EM coupling among the cascaded layers can enlarge the transmission variation range and improve the transmission coefficient [40–44]. Here, three-layer cascaded element is chosen as the basic element, as the topology shown in **Figure 23(a)**. The basic element consists of three identical metallic layers and two intermediate dielectric layers. The commonly F4B substrate is used with a thickness $h = 1.5$mm, dielectric constant $\varepsilon_r = 2.65$, and the loss tangent $\tan\delta = 0.001$. We note that although the metallic mesh is not an absolutely necessary element in designing our basic element, its presence can significantly reduce the mutual couplings between adjacent subunit cells, which make our design robust and reliable. The cell has a lattice of $Px \times Py = 11$ mm $\times$ 11 mm. We can tune the length d_x and d_y of the inner patch to manipulate the transmission spectra along the x- and y-directions, respectively. We adopt the commercial FDTD solver CST Microwave Studio to obtain the EM property of our element. In simulation, the perfect electric conductor (PEC) boundary conditions are assigned along the x- or y-directions for the horizontally polarized wave or vertically polarized wave, respectively. The absorbing boundary condition is applied along the z-direction, as the simulation setup shown in **Figure 23(b)**.

To obtain the transmission spectra of the basic element, we chose a typical element with $d_x = d_y = 8.28$ mm. Illuminated by a horizontally polarized plane wave, the transmission magnitude and phase of the element are presented in **Figure 24(a)**. There exists a relatively wide transparency window between 5.4 and 10.35 GHz, and the transmission phase changes smoothly from -131 to -623° within the transparency window. To realize beam deflection for differently polarized waves, different phase gradients along the x- and y-directions should be satisfied. Here, the phase gradients along the x- and y-directions are arranged as $\xi = 0.45\,k_0$ and $\xi = -0.45\,k_0$, respectively, corresponding to 60° phase increment at the x-axis and a 60° phase reduction at the y-axis. By carefully tuning d_x and d_y, the spectra of the chosen elements are shown in **Figure 24(b)**. The transmission coefficients for each chosen element are higher than 0.8, which guarantees a high efficiency of the elements. The polarization-independent property of the element is essential in determining the working efficiency of the device. We verify the polarization-independent property by scanning the parameter d_x from 3 to 8 mm in steps of 1 mm under excitation of different polarizations. As seen from **Figure 25(a)**, the range of about 330° phase variation is obtained as d_x changes for the horizontal polarization, while it is
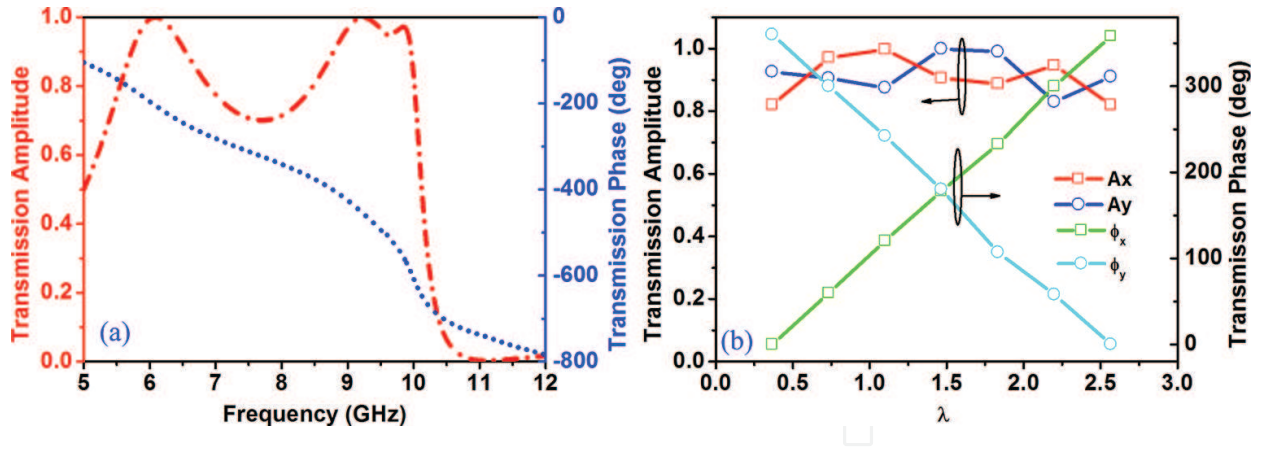
Figure 24. FDTD calculated transmission amplitude and phase for the proposed tri-layer sub-unit cell [38]. (a) Transmission amplitude and phase for the element with $P_x = P_y = 11$ mm, $d_x = d_y = 8.28$ mm; (b) transmission spectra for the elements with 60° phase increment along the x-direction and 60° phase reduction along the y-direction.

about 20° for the vertically polarized transmitted wave. In addition, the transmission amplitude remains better than 0.8 for all cases. We can conclude that the designed element is polarization-independent based on the phase responses to different polarizations with changeable d_x. The good performance of the element provides us possibilities to design PBS with high efficiency. More importantly, with an independent control of different polarizations, bifunctional meta-surface can be designed with very high performances, which shown great advantages over the conventional meta-surfaces.

4.3. Design and analysis of 2D TGMS

With a well-designed element in hand, we can design the TPGM by carefully chosen the elements satisfying the phases both for horizontal and vertical polarizations. A systematical study on the TPGM can provide a guideline for the upcoming PBS design. We derive a four-
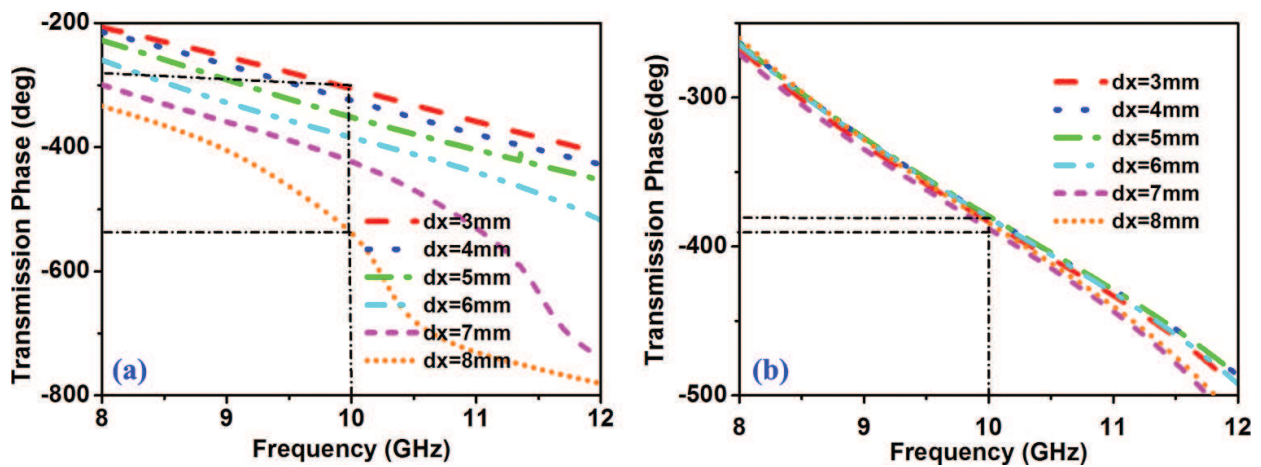

Figure 25. The spectra of transmission phase as functions of frequency and the parameter d_x under excitation of differently-polarized incident waves [38]. The transmission phase response under (a) horizontally polarized and (b) vertically polarized waves.

step design procedure for the general TPGM. For the first step, a transmissive element with a high transmission coefficient and changeable transmission phase should be obtained. Second, the phase distributions at the position (x, y) should be calculated based on the achieving functionalities. Then, the proper subunit cells should be chosen according to the phase distributions. Finally, the EM response of the TPGM should be evaluated by the EM simulator.

Based on derived design procedure, four kinds of TPGM are designed based on the phase distributions, as shown in **Figure 22**. **Figure 26** provides the electric fields distributions of $E_{//}$ and $E_{\wedge}$ at the working frequency of 10 GHz under excitation of a hybrid EM waves. As shown in **Figure 26(a)**, a conventional meta-surface (TPGM1) without phase gradient is launched by a horn antenna. The transmitted wave of both $E_{//}$ and $E_{\wedge}$ propagate along the z-axis, as shown in **Figure 26(b)** and **(c)**. We can conclude that the TPGM1 is impossible to separate the hybrid polarized waves. As $d\varphi_x/dx = -60°$ and $d\varphi_y/dy = 0$ for the TPGM2, horizontally polarized wave is deflected to the angle with $\theta_1 = -27°$, which coincides well with the theoretical value obtained by Eq. (8). However, vertically polarized wave is not deflected. Similarly, horizontally polarized wave propagates along the z-direction while vertical polarization is deflected to the y-direction with $\theta_2 = 27.1°$ for the TPGM3 with the phase distributions $d\varphi_y/dy = 60°$ and $d\varphi_x/dx = 0$. For the TPGM4 shown in **Figure 26(j)** with phase gradients along the x- and y-directions ($d\varphi_y/dy = 60°$ and $d\varphi_x/dx = -60°$), both deflections of $\theta_1 = -27°$ and $\theta_2 = 27°$ are observed by illuminating with differently polarized waves.
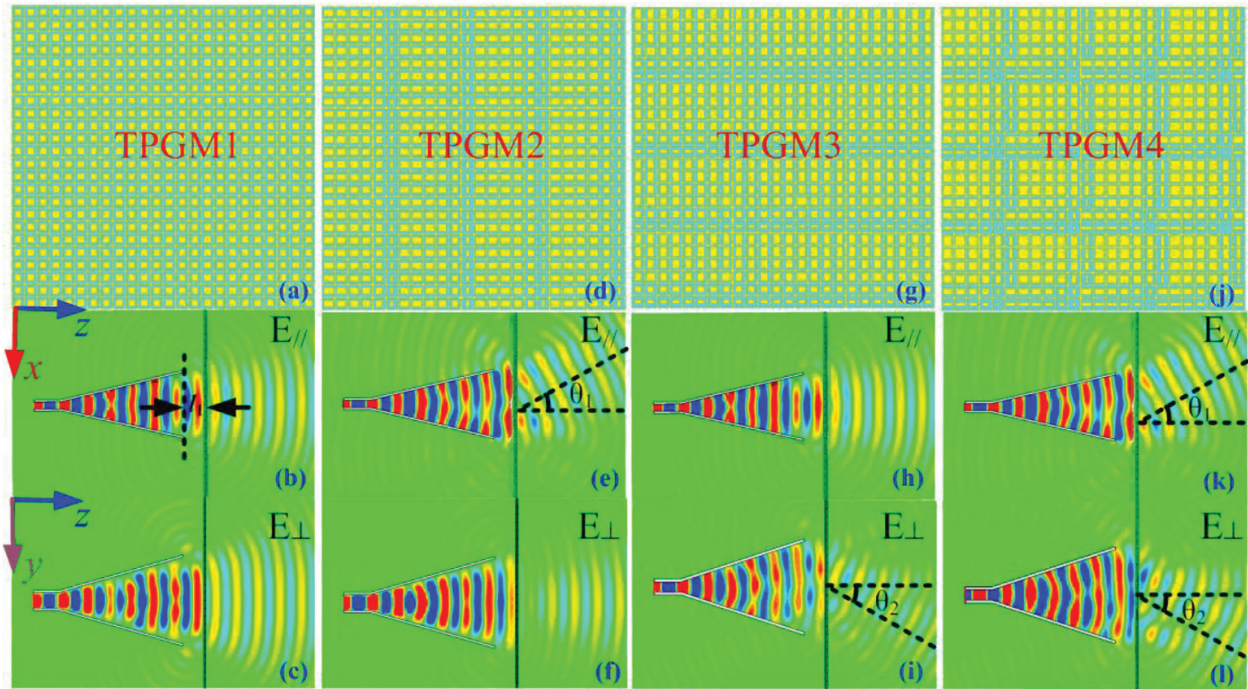

Figure 26. The well-designed four kinds of TPGMs and the results of near-field distributions [38]. The schematics of (a) TPGM1 without phase gradient ($d\varphi_x/dx = d\varphi_y/dy = 0$), (d) TPGM2 with $d\varphi_x/dx = -60°$ and $d\varphi_y/dy = 0$, (g) TPGM3 with $d\varphi_x/dx = 0$ and $d\varphi_y/dy = 60°$ and (j) TPGM4 with $d\varphi_x/dx = -60°$ and $d\varphi_y/dy = 60°$; the electric distributions $E_{//}$ for (b) TPGM1, (e) TPGM2, (h) TPGM3 and (k) TPGM4; the near electric distributions $E_{\wedge}$ for (c) TPGM1, (f) TPGM2, (i) TPGM3 and (l) TPGM4.

4.4. Fabrication and evaluation of PBS

With a well-designed TPGM4, we can further optimize its performance and build a novel PBS by launching the meta-surface by a horn antenna working at the X band. **Figure 27** shows the photograph of the fabricated sample. We can see that 24 × 24 unit cells are adopted for the final PBS, which occupies a total volume of 256 × 256 × 3 mm^3, corresponding to 6.6 λ_0 × 6.6 λ_0 × 0.1 λ_0. It is worth noting that the thickness of the PBS is much smaller than the reported cases. Moreover, the PBS has no complex structures and is fabricated based on the simple print circuit board (PCB) technology. The PBS consists of 4 × 4 super unit cells, as the top and side views of the super unit cell are shown in **Figure 27(a)** and **(b)**. Compared with the working mechanism of the previous PBSs, the designed one is intuitionistic and simple. We can control the differently polarized waves independently due to the different phase gradients at *x*- and *y*-axis, respectively. More importantly, the polarization-independent property of the designed element guarantees the low coupling of different polarizations, which induces a high polarization splitting ratio.

The impedance matching property of the PBS plays an essential role in determining the working efficiency. We evaluate the reflection coefficients of the PBS by launching with different polarizations. First, we assemble the fabricated sample. We used a 20-mm-thick foam plate to support the TPGM and ensure the length l_1 = 20 mm between the TPGM and the horn antenna. The foam has a permittivity near 1 which will not affect the performances of the PBS system. The reflection coefficients are measured by an ME7808A vector network analyzer, and the polarizations of the horn antenna are controlled by the angle θ. The measurement process is shown in **Figure 28(a)**. To obtain a systematical performance of the PBS system, three cases with horizontal, vertical, and hybrid polarizations are considered and measured. Under illuminating of a horizontal polarization with $\theta = 0°$, **Figure 28(b)** provides the simulated and measured reflection coefficients as a function of frequency. There is a good agree-
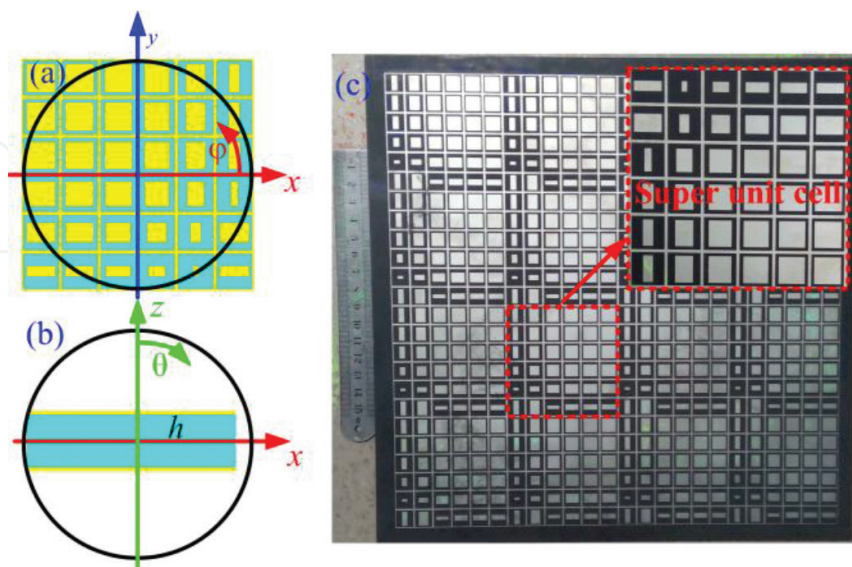

Figure 27. The topology of the unit cell and photograph of the fabricated sample [38]. (a) The top view and (b) the side view of the super unit cell; (c) the photograph of the fabricated sample.
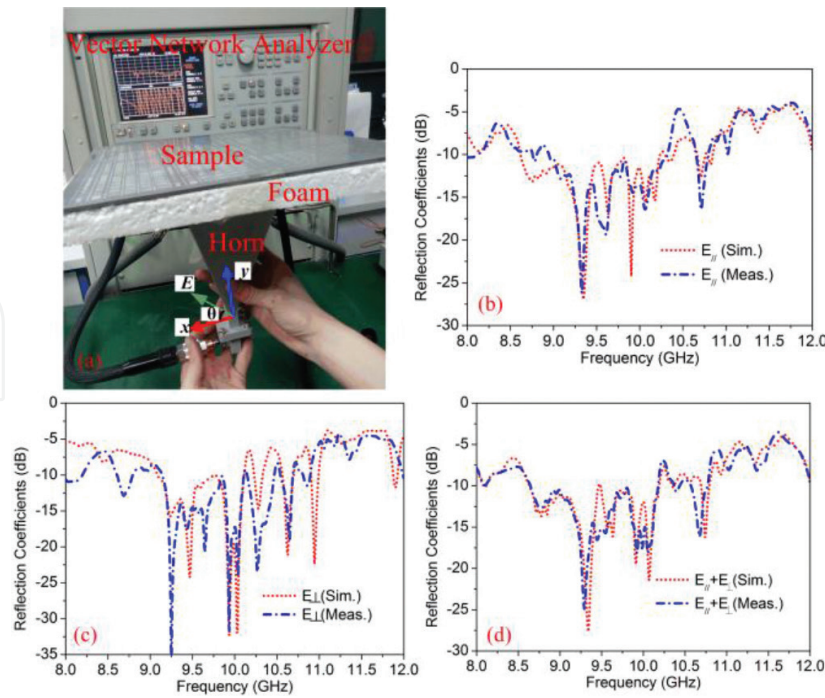
Figure 28. The measurement process of the designed PBS and simulated and measured reflection coefficients for differently polarized incident waves [38]. (a) The measurement process of the designed PBS; the simulated and measured reflection coefficients under illumination of the (b) horizontal, (c) vertical, and (d) hybrid polarizations.

ment between the numerical and measured results. The working bandwidth, ordered by the 10 dB return loss, is about 1.57 GHz (from 8.76 to 10.33 GHz) for the simulation, whereas it is 1.77 GHz (from 8.62 to 10.39 GHz) in measurement. The bandwidth of the PBS is affected by the intersection of the transparency windows of the selected elements. As can be seen from **Figure 28(c)**, the PBS is illuminated by the vertically polarized plane wave with $\theta = 90°$. The slight nonuniformity between the numerical result and measured result is mainly attributed to the fabrication errors. The impedance bandwidth varies from 8.62 to 10.22 GHz and 8.6 to 10.22 GHz for the simulated and measured results, respectively, with the relative bandwidth corresponding to 16.99 and 17.20%. Finally, we rotate the horn antenna by $\theta = 45°$ to obtain a hybrid EM wave. The results are shown in **Figure 28(d)**. The 10-dB impedance bandwidth can be observed clearly as 18.81 and 18.66% for the simulated and measured results, respectively. We can conclude that the designed PBS is insensitive to the polarization of the incident waves, and the PBS has a relatively wide bandwidth.

Then, we examine the 3D far-field patterns of the novel PBS at its working frequency of 10 GHz under excitation of differently polarized waves. Without the TGMS, the horn antenna radiates a narrow beam along the z-direction, which can be demonstrated in **Figure 29(a)**. Shining the TGMS with an x-polarized incident wave, the transmitted beam is deflected to an angle with $\theta_1 = -26.7°$, which is consistent with the theoretical prediction, as shown in **Figure 29(b)**. One point should be highlighted that the side lobe level has not been deteriorated due to the precise design of the PBS. Shining the TGMS with a y-polarized incident wave, the radiation beam propagates along $\theta_2 = 27°$, which shows good agreement with the theoretical value based on Eq. (8) for a second time. Finally, the hybrid polarizations are used
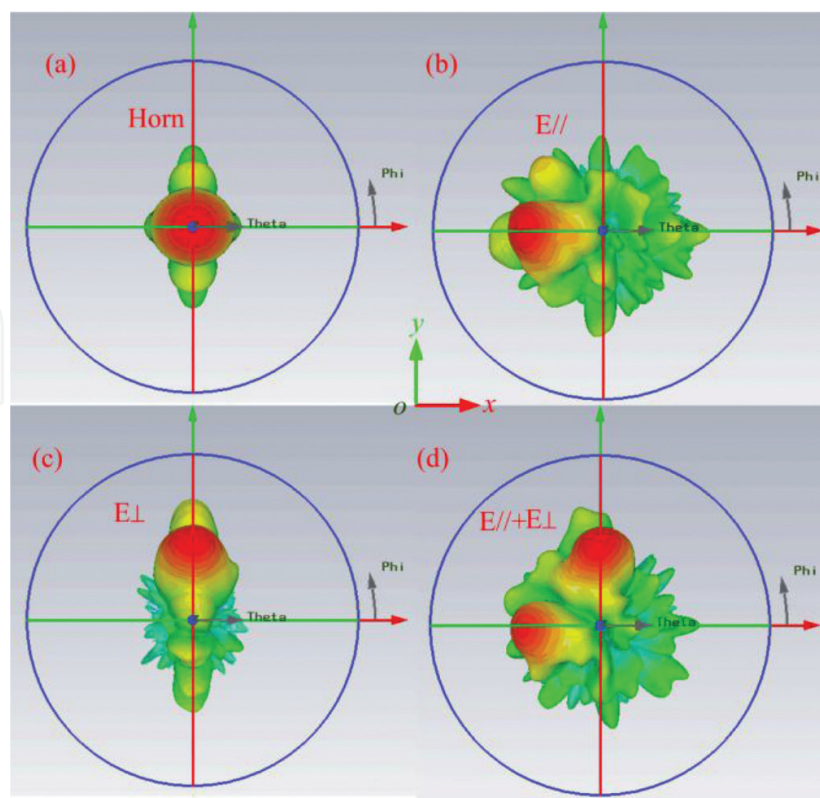
Figure 29. The simulated 3D far-field radiation pattern operating at 10 GHz [38]. (a) The radiation pattern of the bare horn antenna; the 3D patterns of the PBS excited by the (b) horizontally polarized, (c) vertically polarized, and (d) the hybrid polarized waves.

to excite the PBS. **Figure 29(d)** shows two separated beams along the x- and y-directions. Here, two points should be highlighted. First, the two deflected beams have consistent radiation angles with the theoretical values, which demonstrate the reasonable of the PBS design. Second, the radiation dip between the two main lobes is 30 dB lower than that of the radiation peaks, which indicates an excellent polarization splitting performance. To summarize, the well-designed PBC is able to split the orthogonally polarized wave successfully.

Next, we evaluate the 2D radiation patterns of the novel PBS through the far-field measurement system in an anechoic chamber. Here, three excitation polarizations are considered to investigate the far field performances of the designed PBS, as the simulated and measured results shown in **Figure 30**. The measured results coincide well with the simulation except the radiation pattern in the xoy plane as shown in **Figure 30(c)**. The measured beam radiates along $\theta_1 = -30°$, which is slightly departed from the simulated result with $\theta_1 = -27°$. The difference comes from the inherent errors in measurement. In all simulated cases, the levels of the sidelobe are at least 12 dB lower than that of the mainlobe, while it is better than 10 dB for the measured case. Moreover, the front-to-back ratio is about 16 (13) dB for the simulation (measurement). The cross-polarization levels for all cases remain less than 15 dB. The good performances of the designed PBS provide potential applications in wireless communication systems.

The polarization splitting ratio, defined as the radiation gain between two separated radiation beams, is a very important factor for the PBS. We simulate and measure the radiation

patterns at the conical surface θ = -27° to evaluate the polarization splitting ratio. As shown in **Figure 31**, the dip between two radiation peaks is about 30 (18) dB for the numerical (experimental) result, which can evaluate the beam separation degree clearly. Finally, we measure the working bandwidth of the designed PBS by examining the radiation patterns under different polarizations, as the results shown in **Figure 32**. We can see obviously that similar
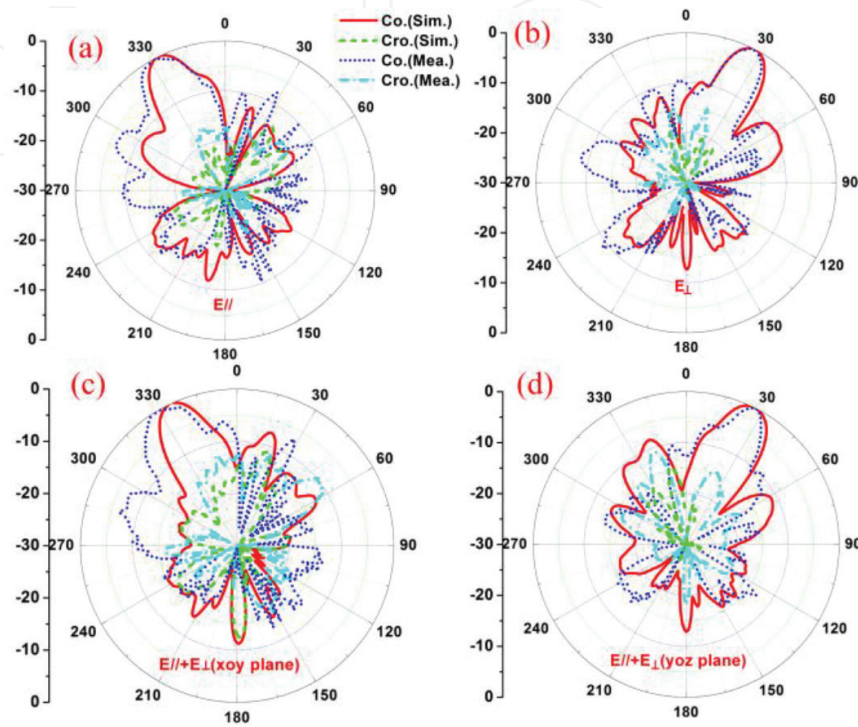

Figure 30. The simulated and measured 2D radiation patterns operating at 10 GHz [38]. The 2D radiation patterns of the PBS excited by the (a) horizontally polarized wave, (b) vertically polarized wave, and (c, d) the hybrid polarized wave.
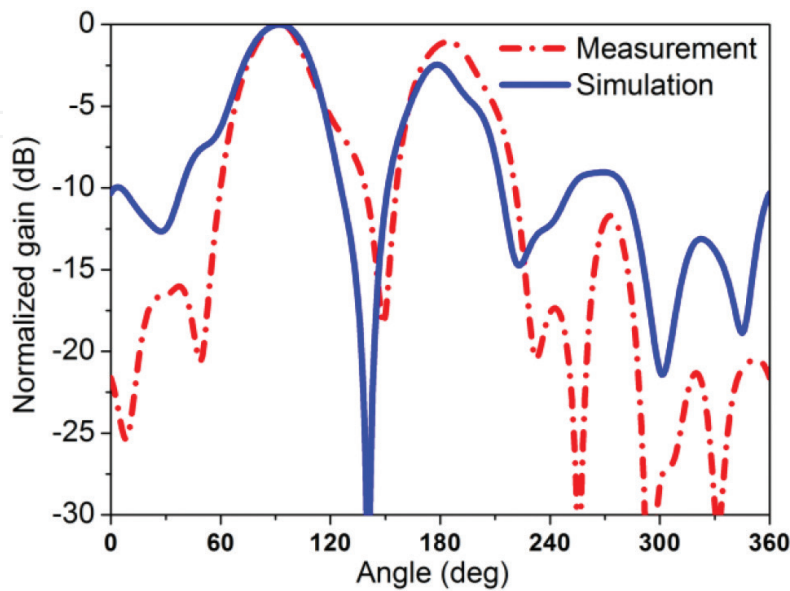

Figure 31. The simulated and measured polarization separation ratios operating at 10 GHz [38].
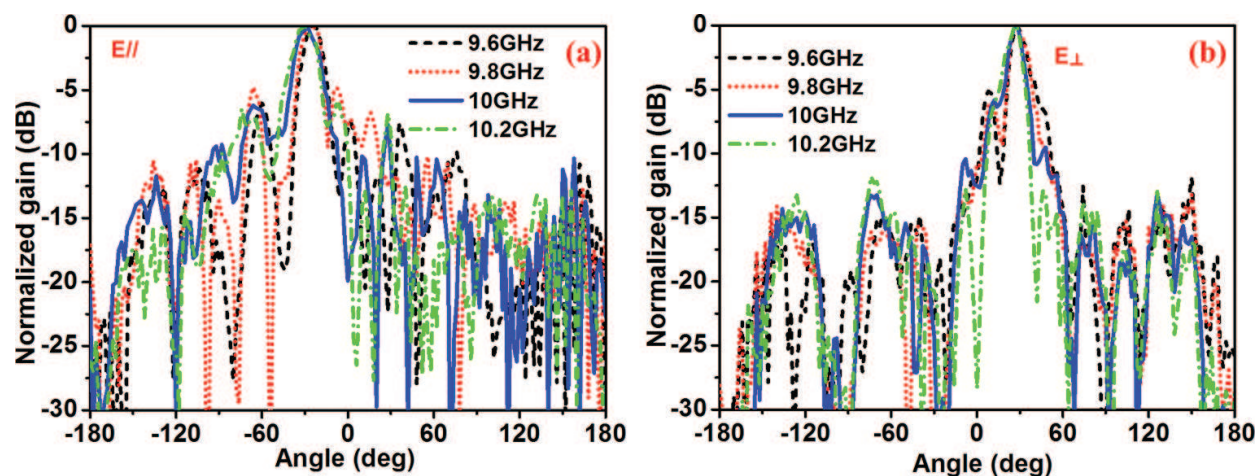
Figure 32. The measured 2D far-field radiation patterns at frequencies changing from 9.6 to 10.2 GHz [38]. The radiation patterns under illumination of (a) TE polarized wave and (b) TM polarized wave.

radiation patterns are detected between 9.6 and 10.2 GHz for both horizontal polarization and vertical polarization, respectively. The half-power beam width (HPBW) is evaluated as about 16° in all cases. The radiation direction of the measured deflected beams varies -26.5° at 9.6 GHz to -28° at 10.2 GHz for the horizontal polarization, while it changes from 27° at 9.6 GHz to 29° at 10.2 GHz for the vertical polarization. The working bandwidth is obtained of about 600 MHz, corresponding to 6%.

In summary, we propose a new strategy to design the PBS aiming at reducing the structure thickness, realizing good polarization splitting ratio, and also high efficiency. A TPGM is proposed based on a carefully designed element, which realizes a high transmission coefficient of more than 0.8, a wide phase variation range over 330° and also a polarization-independent property. The TPGM achieves good beam separation performances as excited by different polarizations. Launched by a wideband horn antenna with a suitable length, an ultra-thin PBS is designed, fabricated, assembled, and measured. Numerical and experimental results show that the PBS can deflect incident waves with different polarizations to different directions with high polarization splitting ratio.

5. Conclusions

In this chapter, we have reviewed our recent efforts in utilizing electrically small meta-surface elements to improve antenna performances and design functional devices, among which three most important aspects have been investigated in depth. First, the constitutive material parameters are controlled by the proposed MED-WG-MS elements, achieving a compact microstrip antenna with enhanced bandwidth. Second, fractal meta-surface and fractal resonator are combined to achieve a CP antenna with a low profile. Third, a high-performance PBS has been proposed based on the TGMS, which shows advances in many aspects such as separating and controlling the orthogonally polarized waves with a polarized splitting ratio better than 18 dB, obtaining a comparable bandwidth of more than 600 MHz, and also gaining

high transmission efficiency. Our results pave a new avenue for both engineers and scientists to realize their devices or demonstrate their findings.

Acknowledgements

Author details

Tong Cai*, He-Xiu Xu*, Guang-Ming Wang and Jian-Gang Liang

*Address all correspondence to: caitong326@sina.cn and hxxuellen@gmail.com

Microwave Laboratory, Air Force Engineering University, Xi'an, China

References

[1] PM. T. Ikonen, S. I. Maslovski, S. A. Tretyakov, et al. "On artificial magneto-dielectric loading for improving the impedance bandwidth properties of microstrip antennas," *IEEE Trans. Antennas Propag.*, Vol. 54, No. 6, pp. 1654–1662, 2006.

[2] X. M. Yang, Q. H. Sun, T. J. Cui, et al. "Increasing the bandwidth of microstrip patch antenna by loading compact artificial magneto-dielectrics," *IEEE Trans. Antennas Propag.*, Vol. 59, No. 2, pp. 373–378, 2011.

[3] H. Mosallaei, K. Sarabandi. "Design and modeling of patch antenna printed on magneto-dielectric embedded-circuit metasubstrate," *IEEE Trans. Antennas Propag.*, Vol. 55, pp. 45–52, 2007.

[4] H. Mosallaei, K. Sarabandi. "Magneto-dielectrics in electromagnetics: concept and applications," *IEEE Trans. Antennas Propag.*, Vol. 52, No. 6, pp. 1558–1567, 2004.

[5] X. M. Yang, X. G. Liu, X. Y. Zhou, T. J. Cui, "Reduction of mutual coupling between closely packed patch antennas using waveguided metamaterials," *IEEE Antennas Wireless Propag. Lett.*, Vol. 11, pp.389–392, 2012.

[6] T. Cai, G.-M. Wang, F.-X. Zhang, et al. "Compact microstrip antenna with enhanced bandwidth by loading magneto-electro-dielectric planar waveguided metamaterials," *IEEE Trans. Antennas Propag.*, Vol. 63, No. 5, pp. 2306–2311, 2015.

[7] C. A. Balanis. Antenna theory: analysis and design, 2nd ed., New York: Wiley, 1997, ch. 14, pp. 36–752.

[8]   T. Cai, G.-M. Wang, J.-G. Liang. "Analysis and design of novel 2D transmission line metamaterial and its application to compact dualband antenna," *IEEE Antennas Wireless Propag. Lett.*, Vol. 13, pp. 555–558, 2014.

[9]   H.-X. Xu, G.-M. Wang, M.-Q. Qi, L.-M. Li, T.-J. Cui, "Three-dimensional super lens composed of fractal left-handed materials," *Adv. Opt. Mater.,* Vol. 1, pp. 495–502, 2013.

[10] D. R. Smith, S. Schultz, P. Markos, C. M. Soukoulis, "Determination of effective permittivity and permeability of metamaterials from reflection and transmission coefficients," *Phys. Rev. B*, Vol. 78, No. 12, pp. 121102, 2008.

[11] X. D. Chen, T. M. Grzegorczyk, B. I. Wu, et al. "Robust method to retrieve the constitutive effective parameters of metamaterials," *Phys. Rev. E*, Vol. 70, pp.016608, 2004.

[12] H.-X. Xu, G. -M. Wang, Q. Liu, J.-F. Wang, J.-Q. Gong, "A metamaterial with multi-band left handed characteristic," *Appl. Phys. A,* Vol. 107, No. 2, pp. 261–268, 2012.

[13] M. A. Antoniades, G. V. Eleftheriades, "A folded-monopole model for electrically small NRI-TL metamaterial antennas," *IEEE Antennas Wireless Propag. Lett.,* Vol. 7, pp.425–428, 2008.

[14] L.-W. Li, Y.-N. Li, T.-S. Yeo, et al. "A broadband and high-gain metamaterial microstrip antenna," *Appl. Phys. Lett.*, Vol. 96, pp. 164101, 2010.

[15] B.-C. Park, J.-H. Lee. "Omnidirectional circularly polarized antenna utilizing zeroth-order resonance of epsilon negative transmission line," *IEEE Trans. Antennas Propag.*, Vol. 59, No. 7, 2717–2720, 2011.

[16] R. L. Li, J. Laskar, M. M. Tentzeris, "Broadband circularly polarized rectangular loop antenna with impedance matching," *IEEE Microw. Wireless Compon. Lett.*, Vol.16, No. 1, pp. 52–54, 2006.

[17] S.-T. Ko, B.-C. Park, J.-H. Lee, "Dual-band circularly polarized patch antenna with first positive and negative modes," *IEEE Antennas Wireless Propag. Lett.*, Vol. 12, pp.1165–1168, 2013.

[18] K.-P. Yang, K.-L. Wong, "Dual-band circularly-polarized square microstrip antenna," *IEEE Trans. Antennas Propag.*, Vol. 49, No. 3, pp. 377–382, 2001.

[19] A. Vallecchi, J. R. D. Luis, F. D. Flaviis, "Low profile fully planar folded dipole antenna on a high impedance surface," *IEEE Trans. Antennas Propag.*, Vol. 60, No. 1, pp. 51–62, 2012.

[20] Y. Dong, H. Toyao, T. Itoh, "Compact circularly-polarized patch antenna loaded with metamaterial structures," *IEEE Trans. Antennas Propag.*, Vol. 59, No.11, pp. 4329–4333, 2011.

[21] S. X. Ta, I. Park, R. W. Ziolkowski, "Circularly polarized crossed dipole on an HIS for 2.4/5.2/5.8-GHz WLAN application," *IEEE Antennas Wireless Propag. Lett.*, Vol. 12, pp. 1464–1467, 2013.

[22] H. Mosallaei, K. Sarabandi. "Antenna miniaturization and bandwidth enhancement using a reactive impedance substrate," *IEEE Trans. Antennas Propag.*, Vol. 52, No. 9, pp. 2403–2414, 2004.

[23] K. Agarwal, Nasimuddin, A. Alphones, "RIS-based Compact Circularly Polarized Microstrip Antennas," *IEEE Trans. Antennas Propag.*, Vol. 61, No.2, pp. 547–554, 2013.

[24] L. Bernard, G. Chertier, R. Sauleau, "Wideband circularly polarized patch antennas on reactive impedance substrates," *IEEE Antennas Wireless Propag. Lett.*, Vol. 10, pp. 1015–1018, 2011.

[25] K. Agarwal, Nasimuddin, A. Alphones, "Triple-band compact circularly polarized stacked microstrip antenna over reactive impedance meta-surface for GPS applications," *IET Microw. Antennas Propag.*, Vol. 8, No. 13, pp. 1057–1065, 2014.

[26] K. Agarwal, Nasimuddin, A. Alphones, "Wideband circularly polarized AMC reflector backed aperture antenna," *IEEE Trans. Antennas Propag.*, Vol. 61, No. 3, pp. 1455–1461, 2013.

[27] K. Agarwal, Nasimuddin, A. Alphones, "Design of compact circularly polarized microstrip antennas using meta-surfaces," *43rd European Microwave Conference (EuMC'2013)*, Nuremberg, pp. 1067–1070.

[28] H.-X. Xu, G.-M. Wang, M. Q. Qi, "Compact dual-band circular polarizer using twisted Hilbert-shaped chiral metamaterial," *Opt. Express*, Vol. 21, No. 21, pp. 24912–24921.

[29] T. Sato, K. Shiraishi, K. Tsuchida, et al. "Laminated polarization splitter with a large split angle," *Appl. Phys. Lett.*, Vol. 61, pp. 2633–2634, 1992.

[30] T. Cai, G.-M. Wang, F.-X. Zhang, J.-P. Shi. "Low-profile compact circularly-polarized antenna based on fractal metasurface and fractal resonator," *IEEE Antennas Wireless Propag. Lett.*, Vol. 14, pp. 1072–1076, 2015.

[31] J. Sun, J. Li. "Terahertz wave polarization splitter using full band-gap photonic crystals," *J. Infrared Millim. Terahertz Waves*, Vol. 36, No. 3, pp. 255–261, 2015.

[32] S. Harish, X. Xu, H. Amir, et al. "Recent advances in silicon-based passive and active optical interconnects," *Opt. Express*, Vol. 23, No. 3, pp. 2487–2510, 2015.

[33] J. Hyung Lee, J. W. Yoon, M. J. Jung, et al. "A semiconductor metasurface with multiple functionalities: A polarizing beam splitter with simultaneous focusing ability," *Appl. Phys. Lett.*, Vol. 104, pp. 233505, 2014.

[34] Y. Xu, J. Xiao, X. Sun. "Proposal for compact polarization splitter using asymmetrical three-guide directional coupler," *IEEE Photon. Technol. Lett.*, Vol. 27, No. 6, pp. 654–657, 2015.

[35] J. Zhao, Y. Chen, Y. Feng. "Polarization beam splitting through an anisotropic metamaterial slab realized by a layered metal-dielectric structure," *Appl. Phys. Lett.*, Vol. 92, pp. 071117, 2008.

[36] H. Luo, Z. Ren, W. Shu, et al. "Construct a polarizing beam splitter by an anisotropic metamaterial slab," *Appl. Phys. B*, Vol. 87, pp. 283–287, 2007.

[37] H. F. Ma, G. Z. Wang, W. X. Jiang, et al. "Independent control of differently-polarized waves using anisotropic gradient-index metamaterials," *Sci. Rep.*, Vol. 4, pp. 6337, 2014.

[38] T. Cai, G.-M. Wang, F.-X. Zhang, et al. "Ultra-thin polarization beam splitter using 2D transmissive phase gradient metasurface," *IEEE Trans. Antennas Propag.*, Vol. 63, No. 12, pp. 5629–5636, 2015.

[39] N. Yu, P. Genevet, M. A. Kats, et al. "Light propagation with phase discontinuities: generalized laws of reflection and refraction," *Science,* Vol. 334, pp. 333–338, 2011.

[40] C. Pfeiffer and A. Grbic. "Cascaded metasurfaces for complete phase and polarization control," *Appl. Phys. Lett.*, Vol. 102, pp. 231116, 2013.

[41] J. R. Cheng and H. Mosallaei. "Optical metasurfaces for beam scanning in space," *Opt. Lett.*, Vol. 39, No. 9, pp. 2719–2721, 2014.

[42] J. Luo, H. Yu, M. Song, et al. "Highly efficient wavefront manipulation in terahertz based on plasmonic gradient metasurfaces," *Opt. Lett.*, Vol. 39, No. 8, pp. 2229–2231, 2014.

[43] Z. Wei, Y. Cao, X. Su, et al. "Highly efficient beam steering with a transparent metasurface," *Opt. Lett.*, Vol. 21, No. 9, pp. 10739–10745, 2013.

[44] Y. F. Li, J. Q. Zhang, S. B. Qu, et al. "Wideband radar cross section reduction using two-dimensional phase gradient metasurfaces," *Appl. Phys. Lett.*, Vol. 104, pp. 221110, 2014.